Solid State Nuclear Magnetic Resonance 143 (2026) 102091

Contents lists available at ScienceDirect

Solid State Nuclear Magnetic Resonance

journal homepage: www.elsevier.com/locate/ssnmr

Nuclear hyperfine interactions in critical metal AlB_2-structured diborides and correlations to physical properties

Timothy J. Bastow [a,1], Anita J. Hill [a,*], Aaron Seeber [a], Katherine M. Nairn [b], Sean T. Holmes [c,d], Robert W. Schurko [c,d,1], Adrian Trinchi [a], Roger J. Mulder [a], Mark E. Smith [e,**]

[a] CSIRO Manufacturing, Stewart Bastow Building, Clayton, Victoria, 3169, Australia
[b] Department of Materials Engineering, Monash University, Victoria, 3800, Australia
[c] Department of Chemistry & Biochemistry, Florida State University, Tallahassee, FL, 32306, United States of America
[d] National High Magnetic Field Laboratory, Tallahassee, FL, 32310, United States of America
[e] Vice-Chancellor and President's Office and Department of Chemistry, University of Southampton, Southampton, SO17 1BJ, United Kingdom

ARTICLE INFO

Handling Editor: Olivier Lafon

Keywords:
NMR
NQR
Hyperfine interactions
DFT
Critical metal diborides
Bonding
Hardness
Catalytic activity

ABSTRACT

Nuclear magnetic resonance (NMR) measurements of the hyperfine parameters (quadrupolar, shifts) at the metal and boron sites are reported from an isomorphous set of eleven stable AlB_2 structure-type space group 191 metal diborides, the main group metal diborides MgB_2 and AlB_2, and transition metal diborides ScB_2, TiB_2, VB_2, CrB_2, YB_2, ZrB_2, NbB_2, HfB_2, TaB_2. Nuclear quadrupole resonance (NQR) studies were performed to locate resonances from ^{177}Hf and ^{181}Ta in the respective diborides. The electric field gradients, V_{zz}, nuclear quadrupole coupling constants, C_q, and Knight shift values, K_{iso}, at the both the metal and boron sites, are reported and are discussed in terms of current state-of-the-art quantum chemical first-principles calculations, as well as being correlated with electronic and cohesive properties of these materials. New experimental results and calculations are presented in addition to re-analysis of existing literature data to test hypotheses of how structure and composition can be tailored to achieve desired physical properties. This comprehensive set of experimental NMR data provides a direct link between measurable hyperfine parameters, calculated bonding parameters, and important physical properties including catalytic activity and asymptotic bulk hardness. The use of magnetic resonance for detection of critical metal diborides via their hyperfine interactions and linking these interactions to physical characteristics opens improved pathways for materials design with novel properties, as well as a method to fingerprint material signatures useful in the circular economy for resource identification, verification, recovery, and reuse.

1. Introduction

1.1. Materials background

Notwithstanding that the metal diborides have constituted a focus of government and industry sponsored atomic energy and space-race research since mid-last century [1–3], the bonding that gives rise to their high-performance properties remains a subject of interest. Metal diborides of the hexagonal hP3 C32 AlB_2 structure-type SG-191 (Fig. 1) possess important combinations of properties, including high melting point, high thermal conductivity, hardness, chemical stability, electrochemical and surface quantum properties, and high heats of combustion, that make them attractive for applications in demanding environments [4–6]. The metals of the isomorphous series examined here have been declared critical metals in Australia, the UK, and the USA, making this series an excellent testbed for remote detection techniques for the optimisation of critical metal processing, separation, and recycling [7, 8]. The cohesive properties of materials depend on the bonding states

This article is part of a special issue entitled: Reimer Special Issue published in Solid State Nuclear Magnetic Resonance.

* Corresponding author.
** Corresponding author.
E-mail addresses: anita.hill@csiro.au (A.J. Hill), m.e.smith@soton.ac.uk (M.E. Smith).

[1] Deceased.

https://doi.org/10.1016/j.ssnmr.2026.102091
Received 15 January 2026; Received in revised form 17 April 2026; Accepted 20 April 2026
Available online 21 April 2026

that can be probed by measuring the quadrupole interaction determined by the electric field gradient (EFG) at the metal and boron sites in this series. The electrical properties of metals are influenced by the conduction electrons near the Fermi surface that can be probed using the Knight shift. This paper studies the ability of solid-state nuclear magnetic resonance (NMR) characterisation coupled with *ab initio* quantum chemical calculations to better understand and predict the structural and electronic properties of these diborides.

This set of eleven stable isomorphous metal diborides encompasses main group metals and transition metals of Groups II, IIIA, III, IV, V, and VI, with melting temperatures from 1268 to 3380 °C, asymptotic bulk hardness values from 12.8 to 25.0 GPa, cohesive energies from −5 to −9 eV/atom, and densities from 2.6 to 12.6 g/cm^3. In general, the higher the melting temperature, the higher the hardness and cohesive energy of these diborides [9]. The high melting temperatures, high hardness, electrocatalytic activity, and energy density of these materials have stimulated theoretical studies aiming to predict and thereby understand the bonding that gives these desirable properties [9–15]. Experimental studies of the bonding in this isomorphous series of metal diborides are scarce. Most studies are theoretical, and the experimental studies typically examine only a few compounds rather than the entire isomorphous set. The range of properties in this isomorphous series facilitates materials design strategies to tailor performance, once the fundamental structure-property relationships are understood. The present study contributes new experimental and computational data on the quadrupole interactions for the entire series of eleven metal diborides.

Dozens of metals (current estimates range from 28 to 32) form MB_2 metal diboride compounds with a variety of structures [16–19]. At least eleven stoichiometric metal diboride compounds form the stable AlB_2 crystal structure *P6/mmm* (SG-191; Mg, Al, Sc, Ti, V, Cr, Y, Zr, Nb, Hf, Ta) at room temperature [20], a hexagonal layered structure with the metal atoms in the plane z = 0 and the boron atoms in a graphite-like layer in the plane z = ½ (Fig. 1). In the literature, the term 'honeycomb-like' boron layer for metal diborides can refer to the AlB_2 structure-type *P6/mmm* (SG-191), Fig. 1, with the boron atoms flat in the plane, and to several variant structures found in diborides, such as that of WB_2 hexagonal $P6_3/mmc$ (SG-194) and MoB_2 trigonal rhombohedral $R\,\bar{3}\,m$ (SG-166), [Supplementary Table S1], with bent, puckered, or corrugated sheets of B rings. The stoichiometry and synthesis conditions can alter the structure. For example, it has been proposed that TaB_2 can possess three stable structures (hexagonal *P6/mmm*, hexagonal $P6_3/mmc$, and orthorhombic *Pmmn*) depending on synthesis pressures and temperatures [21]. Therefore, it is important to confirm the structure and phase purity by X-ray diffraction (XRD). AlB_2-type, MoB_2-type, and WB_2-type structures are readily distinguished by XRD and by NMR because only the AlB_2-type structure with flat boron planes has a single boron site in the unit cell (see Fig. 1 and Supplementary Table S1). Simulations of the XRD powder patterns show this clear distinction of the three structures (Supplementary Fig. S2). Powder XRD data (Supplementary Fig. S3) for the samples examined here confirm the AlB_2-type structure and sample purity.

This isomorphous AlB_2-type series serves as a testbed to monitor how closely current state-of-the-art density functional theory (DFT) calculations can reproduce experimentally measured values of the EFG at the metal and boron sites. There have been some early low field measurements of the NMR interaction parameters for ^{11}B and some of the metals (^{27}Al, ^{45}Sc, ^{51}V). These earlier studies included low magnetic field (0.5 to 2 T) continuous wave (CW) NMR methods in the 1950s to 1970s [22–30]. This paper reanalyses previously reported data using the most up to date parameters such as the quadrupole moment and reports some new higher field nuclear magnetic resonance (NMR) and zero-field nuclear quadrupolar resonance (NQR) data. This analysis is used as the basis to establish the ability to better understand and predict the structural and electronic properties of these diborides using solid-state NMR/NQR characterisation coupled with *ab initio* quantum chemical calculations for the entire set of isomorphous metal diborides.

1.2. Background to magnetic resonance interactions and bonding

There are a range of interactions that affect the splitting of the nuclear spin energy levels, with the most relevant here being dipolar, Knight shift, and quadrupolar [31]. In these metal diborides, both metal (M) and boron (B) atomic sites can be examined by magnetic resonance approaches. For the quadrupolar interaction the EFG interacts with the quadrupolar moment (Q), which is present for nuclei with spin (I) > ½. The quadrupolar interaction is characterised by two parameters, the quadrupolar coupling constant (C_q) and the asymmetry parameter (η) which are measures of the departure from spherical and axial symmetry of the EFG tensor of the relevant nucleus in the crystal structure, respectively. In the case of the hexagonal AlB_2-type crystal structure, the axial symmetry of the metal and boron sites (see Fig. 1) is expected to

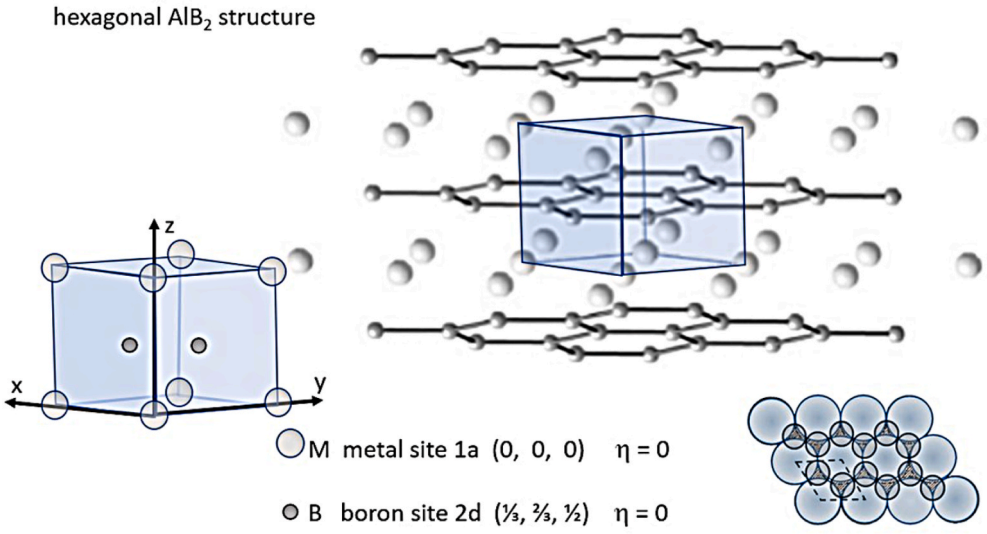

Fig. 1. Schematic showing the hexagonal hP3 AlB_2 structure-type (*P6/mmm* (SG-191)) crystal structure C32 for this set of eleven stable isomorphous metal diborides. The boron sheets are planar as shown in the extended side view. The primitive cell illustrates atomic positions and axial symmetry of metal (M) and boron (B) sites giving an asymmetry parameter η = 0, with one formula unit per primitive cell. The z-axis view shows close packed M atoms, hexagonal graphite-like layer of B atoms, and the unit cell dimension.

give η = 0. If either the first-order structure of the non-central, i.e. not the (1/2, −1/2), transitions or the second-order structure of the central transition can be discerned, then the quadrupolar frequency (ν_q) can be extracted, with its relation to C_q depending on spin I (Supplementary Table S4). Such spectral structure is usually visible in highly crystalline, stoichiometric materials. When such structure cannot be observed, the second-order perturbed central line width Δ (FWHM) can be used to provide an upper estimate of C_q via [31,32]:

$$\Delta = \left[25\left(\nu_q^2\right) \Big/ 144\ \nu_L\right][I(I+1) - 3/4],$$
$$\text{where } \nu_q = 3C_q \left\{\sqrt{[1 + (\eta^2/3)]}\right\} \Big/ [2I(2I-1)] \qquad \text{(Eq. 1)}$$

and where ν_L is the Larmor frequency.

These eleven diborides present a rich range of NMR-active nuclei. Their intrinsic NMR properties are widely varying (Supplementary Table S5). As a key aim of this work is to relate magnetic resonance parameters extracted from experiments to structural/bonding features, the EFG potentially plays a central role. Knowledge of Q is required for the EFG to be determined. Since the present work compares new data with literature EFG data, it is worth noting that some of the previous calculations used Q values which have subsequently been revised, thereby changing the derived EFG. Some of the most recent values of Q (±2%) for quadrupolar nuclei have been estimated and tabulated by Pyykkö [33] and are reproduced for the nuclei present in this set of metal diborides (Supplementary Table S5). Comparing the 2018 values for Q with those determined in 1976, it can be noted that some values have changed by up to 45% over that period, thus highlighting the importance of on-going comparisons of measurement and theory in the study of nuclear hyperfine interactions (Supplementary Table S6).

Recent progress in the use of DFT methods [34] for calculating the isotropic NMR shielding (Knight shift, K_{iso}) in metals [35] has shown that, in general, the shift for main group metals is dominated by the spin contribution, while transition metals require both orbital and spin contributions to adequately reproduce the shielding. A positive K_{iso} means a shift to higher frequencies at constant field. The Knight shift measures the interaction between conduction electrons and atomic nuclei and is proportional to the value of the electron spin density at the nucleus, providing complementary information on the bonding and density of states (DOS). The DOS can be calculated from measurements of susceptibility or electronic specific heat and via theoretical band structure calculations [9,12,36–38]. Comparison of the Knight shift with the DOS and electronic specific heat coefficient can help elucidate the bonding environment in metals, as discussed further in Sec. 4.1. In the case of an axially symmetric Knight shift tensor the interaction is fully described by two parameters, the isotropic value K_{iso} and the anisotropy given by the axial component of the shift tensor K_{ax} [31], as discussed further in Sec. 3.5.

1.3. Summary of magnetic resonance observations of AlB_2-type metal diborides

The first CW NMR measurements of AlB_2 structure-type metal diborides were published by Silver [22,23]. Silver discussed first-principles calculations of coupling constants from electron wave functions but did not perform such calculations [22]. First-principles calculations of ^{11}B nuclear quadrupole coupling constants in metal diborides were reported by Malyuchkov and Povitskii [24] and compared with experimental NMR data, acquired using a magnetic field of 0.5 T, on "*high purity single phase material*". These authors presented a comparison between ^{11}B NMR measurements and calculated values of C_q for five metal diborides as well as Mo_2B_5, CrB, and LaB_6. Values of quadrupolar interactions extracted from experimental data were tabulated without presenting any actual NMR spectra for the diborides. These authors state that four of their ^{11}B C_q values were obtained from first-order perturbed satellite singularities in TiB_2, ZrB_2, NbB_2 and TaB_2, with an estimated error of 10%, whilst the ^{11}B C_q value for CrB_2 was estimated from second-order quadrupole effects with a reported approximate error of 38% [24]. There were no NMR measurements of the metal sites in these first reports on metal diborides. As discussed further in Sec. 3.3, with the benefit of spectra from current state-of-the-art measurements, it is extremely unlikely that Malyuchkov and Povitskii [24] observed ^{11}B first-order perturbed satellite singularities for TaB_2 or second-order quadrupole effects for CrB_2. Given the relevant spectra were not published, that data cannot be reanalysed here. For reference, the values obtained in the present work are compared to the values quoted by early researchers (Supplementary Table S7).

Silver and Kushida [25] published CW NMR data on a set of six metal diborides (TiB_2, VB_2, CrB_2, ZrB_2, NbB_2, TaB_2) with the AlB_2 structure, showing spectral data for the ^{11}B central transition in CrB_2 and the first NMR spectrum of a metal site, ^{51}V in VB_2. Schwarz et al. [39] presented a comparison between the previous experimental work [25] and *ab initio* calculated V_{zz} (the largest component of the EFG tensor) values for these six metal diborides. The tabulated experimental values in Schwarz et al. [39] included four ^{11}B measurements of quadrupolar frequency, ν_q, based on ±(1/2, 3/2) satellite singularities, and two ^{11}B measurements based on estimations of upper limits for ν_q from the full width at half maximum (FWHM) of the central transition. Only one experimental V_{zz} for a metal nucleus (^{51}V) was given based on the first-order satellite singularity measured by Silver and Kushida [25,39]. In the original work [25], only three ^{11}B NMR spectra for CrB_2, TiB_2, and ZrB_2 were shown, along with the ^{51}V spectrum for VB_2. Again, reanalysis and comparison of past results are made difficult by the lack of published experimental data.

Pulsed Fourier transform (FT) NMR measurements of the metal and boron sites in AlB_2 structure-type metal diborides have since been reported for individual diborides, MgB_2 [38,40,41], TiB_2 [42], and CrB_2 [43], and there have been reports of ^{11}B studies of the boron sites in several metal diborides [44–46]. However, to date there has been no report of NMR data for the metal and boron sites for this entire isomorphous set of metal diborides, which would allow comparison and testing of hypotheses across this set. Vastly differing hypotheses regarding the nature of the chemical bonds in these AlB_2 structure-type metal diborides ignited the "charge transfer wars" [5,47]. Along the way, many researchers have suggested that NMR measurements of the full isomorphous series would help elucidate the bonding [10,11,25,30,36,47,48].

In the present work, selection of this isomorphous series removes the questions surrounding the role that bent or corrugated boron sheets play in the bonding of AlB_2 structure-type diborides [10,11,30]. However, ongoing subjects of discussion include the relative importance of the B-B covalent network over the M-B and M-M bonds, the covalent and ionic mix of the M-B bonds and the variation of chemical bonding parameters within the Periods and Groups of the Periodic Table for this isomorphous series [5,10,11,13,37,49–56]. An examination of the metal and boron site EFGs and Knight shifts for the elements across the Periodic Table (Groups and Periods) that form diborides with the stable AlB_2-type structure SG-191 can shed additional light on these areas of debate. In the present work, the spectra from previous CW NMR measurements have been revisited and reanalysed, along with new data using pulsed FT NMR with signal averaging at higher field (9.4 T) and by NQR in zero applied field. This work provides a comprehensive spectral data set for this isomorphous metal diboride series spanning Group II, IIIA, III, IV, V, and VI metals for the first time.

CW spectra for quadrupolar nuclei are in the form of the derivative of

signal intensity as a function of frequency ν, i.e. ∂(intensity)/$\partial(\nu)$, versus frequency, and FT NMR spectra are in the form of the intensity as a function of ν (Supplementary Fig. S8). As discussed by Creel [26,57] the value of the reported nuclear quadrupole frequency, ν_q, extracted from the CW data will depend on whether the splitting of the peaks of the derivative or the splitting between the zero crossings of the derivative is measured, or indeed if the average of these two splitting values is used. In general, for the early work on AlB_2-type metal diborides, the work led by Barnes [26–29] used the 'average' method while the work from the Bray group [22,23,25] used the 'peak' method. These spectral analysis variations are further discussed in Sec. 3.2. The FT NMR method relies on the singularities of the satellite transitions to determine the first-order C_q values. If the satellite transitions cannot be detected then the central transition second-order splitting observed for the (1/2, −1/2) singularities can be used to determine C_q values. In such situations our observations show that typically the second-order $C_q(2)$ values are usually within 5-10% of the more accurate first-order $C_q(1)$ values. If central transition singularities cannot be detected then the FWHM of the central peak is used as an upper limit on the value of Δ (Eq. (1)), giving an estimate for $C_q(2)$ typically within 10% of first-order determined $C_q(1)$ values [31].

Analysis of the literature data from the past 65 years shows that variations of up to 30% are observed in NMR experimental values for quadrupolar coupling constants, C_q, reported for seemingly identical AlB_2-structure type metal diboride compounds. Here the most accurate experimental values now available are compared with the current state-of-the-art DFT calculations. Variations observed in the past literature are addressed, which may be attributable to a range of reasons—some of which are refinement of material preparation (sample stoichiometry and purity), measurement technique, analysis method, and improved accuracy of Q. For these reasons, it is important to have carefully documented spectra and NMR parameters for pure phases to assist future research, as metallurgical mechanisms such as strain and defect engineering, alloying, clustering, high entropy, atomically thin 2D materials, and glassy phases are still being systematically explored for tuning these materials for demanding applications.

Measurement strategies using pulsed FT NMR depend on the magnitude of the EFG. As the quadrupole interaction becomes moderately large, C_q ~10 MHz, this gives rise to linewidths that exceed the bandwidth of the probe or the bandwidth that can be excited by the pulse. This challenge can be overcome using echoes, sub-$\pi/2$ pulses, with awareness of the relevant bandwidths, frequency stepping, and long signal averaging times [58–61]. For very large C_q values, NQR approaches are used. In addition to the comprehensive experimental NMR study of this isomorphous set, EFG values are calculated using DFT methods for the metal and boron sites, allowing a full comparison of experiment and theory to be presented for the first time.

2. Experimental details

2.1. NMR at 9.4 T and in zero applied field

All new experimental NMR results in the present work were obtained at room temperature by NMR at 9.4 T using a Bruker 400 MHz spectrometer. In addition, ^{177}Hf and ^{181}Ta NQR spectra, for the respective diborides, were obtained in zero applied field at room temperature. The Larmor resonance frequency (ν_L) for each nucleus at 9.4 T is given in (Supplementary Table S5), along with the reference compounds for zero shift (Supplementary Table S9) where the conversion to the IUPAC shift reference is also quoted. A two-pulse echo sequence with phase cycling was used for recording static NMR spectra with pulse duration of ~4 to 10 μs, pulse separation ~50μs, and pulse repetition rate of 20 to 500 ms depending on the nuclear relaxation rate [40,42,43]. Spectra were obtained by Fourier transforming the whole echo, taking a magnitude correction to give the true absorption lineshape [62]. Broad lines were defined by frequency stepping [58,59]; the width of the pulse was varied to achieve the required pulse bandwidth for the chosen frequency slice, typically 5 μs for a 200 kHz slice using 300 W transmitter power. For zero field measurements, the probe head was a long cylindrical copper pot with an enamelled wire wound coil attached to a home-built matching circuit by a short, low thermal conductivity, transmission line as recently described in detail elsewhere [43].

2.2. Metal diboride powders

Metal diboride samples were received as crystalline powders: MgB_2 (98%) from Alfa Aesar; TiB_2 (97%), ZrB_2 (98%) from H. C. Starck; AlB_2 (99.7%), CrB_2 (99%), TaB_2 (99.5%) from Sigma Aldrich; and HfB_2 from Borax Consolidated Limited. Powder XRD patterns were obtained using a Bruker D8 Advance X-ray diffractometer, using CuKα radiation, and the Bruker XRD search match program Eva was used to identify the matching powder diffraction file (PDF). YB_2 and ScB_2 data are obtained from the work led by R. G. Barnes at Ames Laboratory and Iowa State University [28]. The YB_2 and ScB_2 samples were prepared at Ames Laboratory with X-ray analysis indicating >90 to 95% single phase [26]. In addition, ScB_2 data are obtained from Carter and Swartz [30] on high purity nearly single-phase crystalline powder received from Cerac Inc. with all XRD peaks indexed to confirm the AlB_2 structure-type crystal structure [63]. For ^{51}V in VB_2, data are from Silver and Kushida [25], where the commercial powder from Borolite Corporation was X-rayed to confirm the AlB_2 structure-type crystal structure. For ^{93}Nb in NbB_2, data at 7.05 T are obtained from Su et al. [64] on high purity, high quality commercial powder with all XRD peaks indexed to NbB_2. ^{11}B NMR data for NbB_2 and VB_2 are from Lue and Lai [44] for well-ordered "nearly single-phase" crystalline powders measured at 9.4 T.

2.3. NMR of conducting powders

The metal diborides studied here are electrically conducting materials, so for NMR experiments at 9.4 T the applied rf pulses are attenuated in the surface of the powder particles with a depth of penetration termed the skin depth [31]. Hence only the outer 10 to 20 μm of the powder particles absorbs the rf and generates the NMR spectrum. The as-received powder sample particle size was typically 50 μm or smaller (325 mesh), giving no difficulty in tuning or balancing the probe. If difficulties were encountered, particles were sieved and if needed mixed with non-conducting powders (e.g. MgO, Al_2O_3) to optimize signal and prevent Joule losses in the probe.

2.4. Density functional theory

Calculations were performed using the plane-wave DFT software package CASTEP. The EFG tensors were calculated using the PBE functional with Wu-Cohen (WC) exchange, zeroth order regular approximation (ZORA) ultrasoft pseudopotentials generated on the fly, a plane-wave cut-off energy of 1200 eV, and a k-point spacing of 0.01 $Å^{-1}$. SCF convergence was achieved through the All-Bands/EDFT minimizer using a threshold of 5×10^{-8} eV $atom^{-1}$. The plane-wave DFT inherently accounts for the long-range periodic order of the crystal structures [65]. The asymmetry parameter η for the metal and boron sites in these metal diborides was zero due to crystal site symmetry. The plane-wave DFT calculations performed in CASTEP strictly enforce crystallographic symmetry constraints. Therefore, the value of the asymmetry parameter was required to be precisely zero in these calculations. If instead a calculation were run that did not enforce these requirements (e.g., by creating a supercell with P1 symmetry), it is probable that the

asymmetry parameter would slightly deviate from zero. As the sign of the quadrupole coupling constant at the nucleus C_q cannot be determined from NMR measurements, absolute values of experimentally observed and theoretically derived values of C_q (and EFG) are compared.

3. Results

3.1. XRD of metal diboride powders with AlB_2 structure-type

The as-received powder specimens were all highly crystalline, as illustrated by the XRD data and matching powder diffraction files (Supplementary Fig. S3). The as-received purity levels and crystallinity were confirmed by sharply defined diffraction peaks belonging to the metal diboride phase. All samples were high purity with no other phase detected except in a few cases where minor impurities were detected as follows: the MgB_2 powder contained 4.3 ± 0.2 wt% periclase (MgO); the AlB_2 powder contained 5.2 ± 0.3 wt% elemental fcc aluminum (Al) and 2.4 ± 0.4 wt% corundum (Al_2O_3); the CrB_2 powder contained 5.1 ± 0.6 wt% Cr_3B_4; the HfB_2 powder contained 10.1 ± 0.2 wt% hafnium carbide nitride ($HfC_{0.5}N_{0.5}$), 2.1 ± 0.5 wt% cubic hafnium oxide (HfO_2), and 2.9 ± 0.3 wt% monoclinic hafnium oxide (HfO_2).

3.2. First-order C_q measurements and upper limit estimates for C_q from ^{11}B NMR

As introduced in Sec. 1.3, researchers in the 1950s to 1970s used slightly different methods for the analysis of the CW spectra to extract the measured quadrupole splitting parameters from first-order satellite peaks, e.g. peak to peak, zero crossings, or average. Creel [26] noted that the differences in measurement method could lead to differences in quadrupole frequency of 5%, for example in the ^{11}B NMR measurement of ν_q in CrB_2. As computational simulation methods were developed for fitting NMR spectra, direct spectral fitting became a standard approach across the research community in the early 2000s [66–68]. In the present work, we publish the spectra and the measurement method used so that the data from any era can be systematically analysed to extract comparable interaction parameters across this isomorphous set for comparison with theory. Such a compilation of experimental data should assist in future research efforts as measurement, analysis, and theory methods are refined. An overview of previous ^{11}B NMR data collected on these diborides for comparison with the present work is given in (Supplementary Table S10).

Fig. 2 presents a comparison of CW spectra and FT spectra for ^{11}B (I = 3/2) NMR of three metal diborides with the ±(1/2, 3/2) satellite features annotated. The small C_q values for ^{11}B NMR of AlB_2 structure-type metal diborides means that the second-order splitting of the central peak is not observable. The distance between the satellites is the quadrupole frequency, ν_q. The CW data are marked to show how the reported quadrupole frequency, ν_q, was measured in the original publication. The FT NMR data are fitted using DMFIT [67]. In each case in Fig. 2, the FT NMR measurement gives a smaller value (by about 5%) for ν_q and hence C_q. Part of the difference between the FT and CW NMR values may come from the way the authors of the original CW NMR publications chose to measure ν_q (Supplementary Table S11). Part of the difference may be due to improvement in materials synthesis over time. Generally, as higher magnetic fields and more modern electronics are used, the improved signal-to-noise provides more accurate data.

Fig. 3 shows the ^{11}B FT NMR spectra of six other AlB_2 structure-type metal diborides, with the satellite features, if visible, annotated. There is one diboride, HfB_2, shown in Fig. 3 (c), with satellite features only partially resolved due to either disorder or dipolar broadening; however, DMFIT [67] can provide a best fit to the partially resolved satellites. There are two diborides, TaB_2 and NbB_2 shown in Fig. 3 (e) and Fig. 3 (f), where first-order satellite features are not detected. In these cases, the FWHM of the central transition is used to estimate an upper limit for ν_q. Also, to the best of our knowledge, there are no published spectra for ^{11}B NMR in ScB_2 or YB_2, although the values for ν_q have been reported from ^{11}B NMR measurement of satellite peaks by three groups [28,30,69]. As shown in Supplementary Table S10, the reported values for ^{11}B quadrupole coupling constant C_q from the three groups are within 30%.

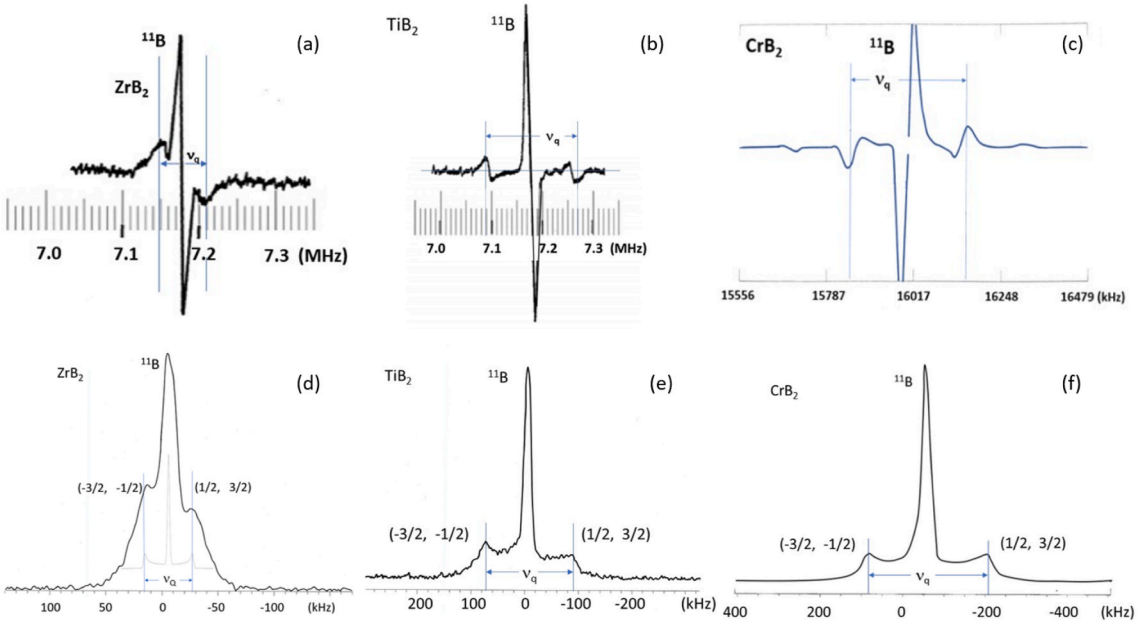

Fig. 2. Comparison of ^{11}B (I = 3/2) CW and FT NMR for three diborides showing the satellite features and first-order singularities giving quadrupole frequency, ν_q, used to calculate the quadrupole coupling constant C_q. (a) ZrB_2 (ν_q = 59 kHz) and (b) TiB_2 (ν_q = 180 kHz) CW data adapted from Silver and Bray [23] ν_L = 7.177 MHz, field is 0.525 T, and (c) CrB_2 (ν_q = 299 kHz) CW data adapted from Creel [26] ν_L = 15.99934 MHz, field is 1.171 T. FT NMR data of the present work at 9.4 T (d) $Zr^{11}B_2$ (ν_q = 44 kHz), (e) $Ti^{11}B_2$ (ν_q = 164.5 kHz), and (f) $Cr^{11}B_2$ (ν_q = 285 kHz). The y-axis is arbitrary intensity. CW convention is higher frequency to the right, whereas FT convention is higher frequency to the left.

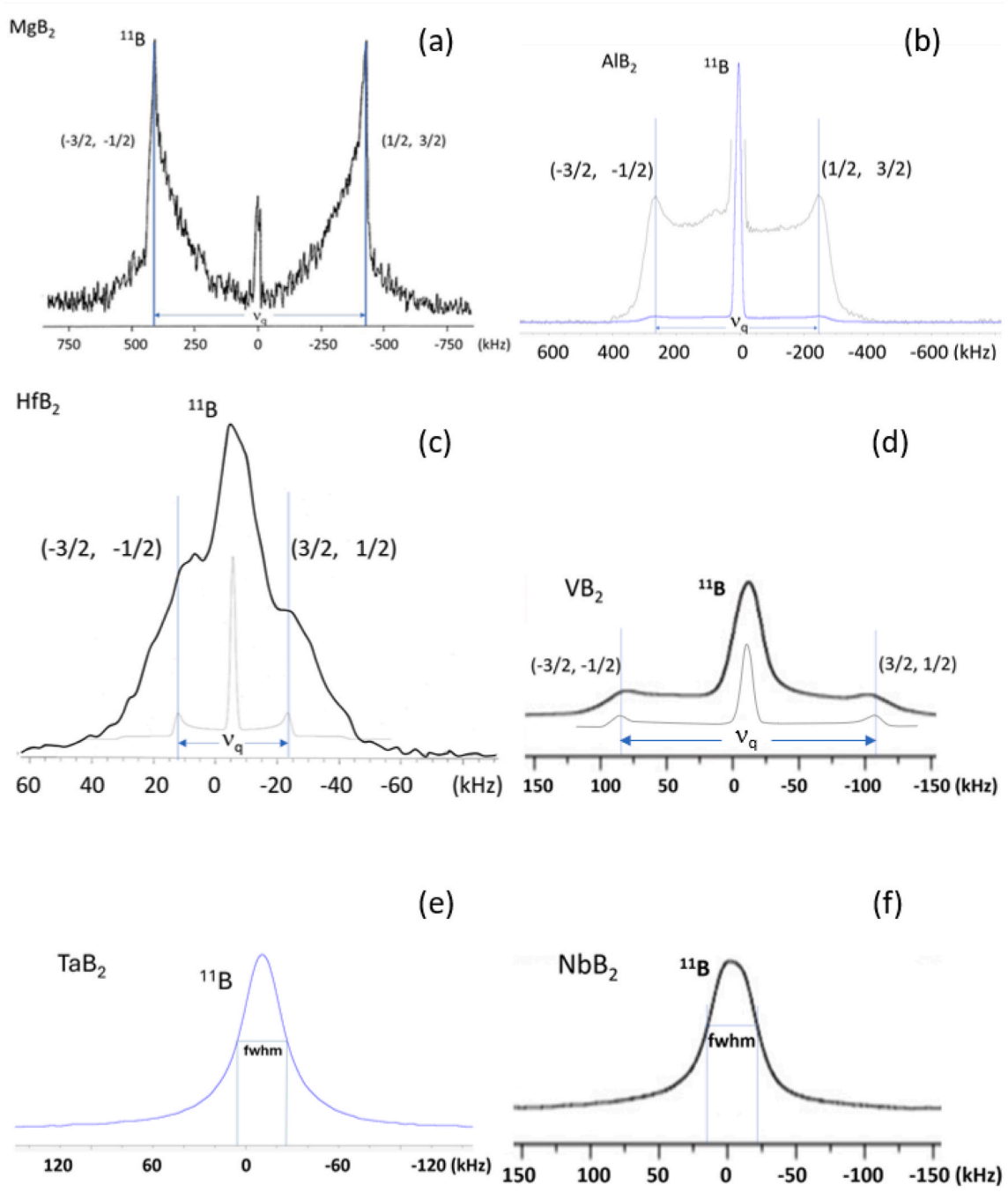

Fig. 3. ^{11}B FT NMR at 9.4 T for (a) MgB_2 showing the ±(1/2, 3/2) satellites and doublet structure of the central peak, adapted from Bastow [40]. (b) AlB_2 showing the ±(1/2, 3/2) satellites, with increased intensity scale on a secondary y-axis to emphasize the satellite singularities. (c) HfB_2 showing the ±(1/2, 3/2) satellites. (d) VB_2 showing the ±(1/2, 3/2) satellites, adapted from Lue and Lai [44]. (e) TaB_2 showing no satellite features, FWHM = 32 kHz. (f) NbB_2 showing no satellite features, FWHM = 40 kHz, adapted from Lue and Lai [44].

There is an issue with the table notes of Carter and Swartz [30] (Table 1 of their 1971 publication), which suggests that wrong gamma values may have been used in the calculation of C_q. Without the original spectra, this issue is impossible to rectify here. Haas [69] did not report the experimental NMR apparatus, nor publish spectra. Due to lack of clarity in the reports from Carter and Swartz [30] and Haas [69], the $Sc^{11}B_2$ and $Y^{11}B_2$ values reported by Barnes et al. [28] are used here.

Table 1 contains the 'best' current ^{11}B C_q and V_{zz} values for each of the diborides determined in the present work. To provide an overview of all the data, Table 1 also has computational ^{11}B values. Additionally, the corresponding C_q and V_{zz} values for the metal nuclei and the Knight shifts for both ^{11}B and the metal, presented in later sections, are stated in Table 1 to give a comprehensive overview of all the key magnetic interaction parameters from this series.

Table 1
The 'best' experimental values determined either from measurements presented here or from reanalysis of the literature data for AlB_2-type MB_2 compounds. The data include the experimental ^{11}B and metal (M) C_q and EFG values, the Knight shift (K_{iso}) data, and our calculated C_q and V_{zz} values. Comprehensive sets of previously determined values are listed in Supplementary Tables S7, S10, S11, S13. All the analysis is based on $\eta = 0$ which should be true for the AlB_2-type crystal structure confirmed by the XRD data.

Compound MB_2	^{11}B					M				
	Experimental C_q (MHz)[a]	Calculated C_q (MHz)	Experimental V_{zz} ($\times 10^{21}$ V/m^2)[b]	Calculated V_{zz} ($\times 10^{21}$V/m^2)[b]	K_{iso} (ppm)	Experimental C_q (MHz)[a]	Calculated C_q (MHz)	Experimental V_{zz} ($\times 10^{21}$ V/m^2)[b]	Calculated V_{zz} ($\times 10^{21}$V/m^2)[b]	K_{iso} (ppm)
MgB_2	1.69 ± 0.01	1.875	1.722	1.911	+81 ± 10	1.49 ± 0.02	−4.81	0.309	−0.998	+260 ± 10
AlB_2	1.022 ± 0.003	1.090	1.041	1.111	+30 ± 10	1.03 ± 0.01	−0.15	0.291	−0.042	+880 ± 10
ScB_2	0.576 ± 0.01[d]	0.656	0.587	0.668	−50 ± 50[d]	5.31 ± 0.25	−5.29	0.998	0.995	+900 ± 100[h]
TiB_2	0.33 ± 0.01	0.411	0.336	0.419	−72 ± 20	14.86[c] (^{47}Ti)	14.23	2.035	1.949	−440 ± 70
						12.35 ± 0.02 (^{49}Ti)	11.76	2.068	1.969	−400 ± 100
VB_2	0.40	0.457	0.408	0.466	−182 ± 60[e]	2.18 ± 0.17	−1.57	1.734	1.249	−3370 ± 30
CrB_2	0.570 ± 0.01	0.667	0.581	0.680	−434 ± 40	2.57 ± 0.25[c]	−1.82	0.709	0.502	−9990 ± 70
YB_2	0.398 ± 0.01[d]	0.439	0.406	0.447	−50 ± 50[d]	NA	NA	NM	0.622	+1600 ± 100[d]
								1.01 ± 0.05[j]		
ZrB_2	0.088 ± 0.002	0.147	0.090	0.150	−76 ± 20	18.47 ± 0.04	−17.12	4.340	4.023	−1472 ± 100
NbB_2	<0.08	0.098[f]	0.082	0.100	−82 ± 10[i]	33.6	38.92[f]	4.342	5.03	−4300 ± 400
HfB_2	0.076	0.153	0.077	0.156	−47 ± 10	721±7[g]	720.2	8.865	8.852	NM
										−2357 ± 400[k]
TaB_2	<0.064 ± 0.006	0.077	0.065	0.078	−111 ± 30	560 ± 5	538.2	7.306	7.022	NM
										−5574 ± 400[k]

NA not applicable as ^{89}Y is a spin-½ nucleus.
NM not measured.
[a] All are determined from the more accurate first-order satellites (see text—in comparison to having to extract from the central transition lineshape or linewidth), except for cases where such structure was not detected.
[b] Using values of Q from Pyykkö [33].
[c] Determined using Δ or fwhm = Δ (Eq. (1)) of the central transition to give an upper estimate.
[d] Barnes et al. [28].
[e] Silver and Kushida corrected for zero shift reference [25].
[f] Schwarz et al. [39].
[g] NQR derived value.
[h] Determined from analysing Fig. 8(b) [26].
[i] Determined by comparison of data of Lue and Lai [44] with data of Silver and Kushida [25] and data of present work (Supplementary Table S13).
[j] Calculated from linear regression best fit relationship between $|V_{zz}|$ of hexagonal hP2 pure metals and hP3 diborides: $|V_{zz(\text{pure metal})}| = 0.9785|V_{zz(\text{diboride})}|$, $R^2 = 0.99$ (Supplementary Table S14 and Fig. S14).
[k] Calculated from linear regression best fit for relationship between $|K_{iso}|$ of pure metals and diborides: $|K_{iso(\text{pure metal})}| = 1.9734|K_{iso(\text{diboride})}|$, $R^2 = 0.93$.

Table 2
Measured melting point, density, crystallographic data, asymptotic bulk hardness, electronic specific heat coefficient, and theoretical cohesive energy and density of states of AlB_2-type metal diborides.

Compound	Melting Point, T_m, (C)	Density (g/cm^3)	Metallic Radius R_M (pm) R_B = 87pm	M-B (Å)	B-B (Å)	M-M (Å)	a (Å)	c (Å)	Cell Volume ($Å^3$)	Vickers hardness, H_V, asymptote (GPa)	Electronic specific heat coefficient, ɣ, (mJ/mol K^2)	Cohesive Energy (eV/atom)	Total density of states at E_F, $N(E_F)$, (states/eV formula unit)	Boron p-electron DOS (states/eV formula unit)	Metal s-,d-electron DOS (states/eV formula unit)	Metal d-band center (eV)
MgB_2	1268	2.67	160	2.505	1.782	3.086	3.086	3.521	29.04	12.8	0.84[a]	−5.12	0.71	0.52	0.19	0.05[b]
AlB_2	1350	3.17	143	2.378	1.735	3.005	3.005	3.253	25.44	13.2	0.57[a]	−5.75	0.31	0.14	0.17	0.17[b]
ScB_2	2250	3.67	162	2.529	1.817	3.148	3.148	3.516	30.18	17.8	2.20	−7.41	0.83	0.25	0.58	0.20
TiB_2	3225	4.38	147	2.381	1.754	3.038	3.038	3.220	25.74	25.0	1.08	−8.17	0.45	0.07	0.38	−0.18
VB_2	2747	5.07	134	2.292	1.731	2.998	2.998	3.005	23.39	20.0	4.84	−8.24	1.24	0.13	1.11	−0.82
CrB_2	2200	5.20	128	2.299	1.714	2.969	2.969	3.066	23.41	15.8	13.60[a]	−6.97	5.00	0.34	4.66	−1.51
YB_2	2100	5.54	180	2.699	1.899	3.290	3.290	3.835	35.95	17.1	2.65	−7.18	0.95	0.25	0.70	0.33
ZrB_2	3200	6.10	160	2.544	1.830	3.170	3.170	3.533	30.75	19.0	0.93	−8.30	0.34	0.08	0.26	−0.24
NbB_2	3050	6.97	146	2.429	1.798	3.115	3.115	3.265	27.44	18.5	2.33	−8.60	1.03	0.24	0.79	−0.86
HfB_2	3380	11.19	159	2.510	1.812	3.139	3.139	3.473	29.64	21.5	1.00	−8.80	0.30	0.08	0.22	−0.43
TaB_2	3200	12.54	146	2.409	1.783	3.088	3.088	3.241	26.76	19.5	2.80	−9.05	0.94	0.26	0.68	−1.45

Metallic Radii from Ref. [76].
Melting point (or peritectic decomposition) temperature and density from Refs. [20,49,77–81].
Lattice parameters, M-B, B-B, M-M from Refs. [13,82].
Vickers hardness asymptotic values from numerous sources as described in main text Sec. 4.2.4 (Supplementary Table S15).
Electronic specific heat coefficient, or Sommerfeld constant ɣ, values from [36, 83, Supplementary Table S16 and Fig. S16].
DOS values from Refs. [12,83].
Calculated cohesive energies from Refs. [84–86].
Weighted average of the energy of the DOS for d-states, the d-band center, calculations from Refs. [15,87].
[a] Normal state value for MgB_2 above superconducting transition at 39K. Antiferromagnetic state value for CrB_2 which is antiferromagnetic below $T_N = 88K$. Calculated value for AlB_2 as no measured value could be found [88].
[b] Extrapolated values for d-like states in MgB_2 and AlB_2 as described in main text Sec. 4.1.

3.3. Early observations of doublet structure of the central ^{11}B peak in diborides

Malyuchkov and Povitskii [24] reported observing a splitting of the central ^{11}B NMR line of CrB_2 and incorrectly attributed this splitting to second-order quadrupole splitting. Silver and Kushida [25] published the CW spectrum of the central line of CrB_2 showing a splitting of the asymmetric central peak of 12.1 kHz consistent with the previous observation, as well as reporting the separation of the first-order quadrupolar satellite singularities, ν_q, of 310 kHz. Silver and Kushida [25] remark that the structure at the center of the ^{11}B line also occurs for VB_2 with the splitting less pronounced at lower fields, and the peak-to-peak linewidth remaining constant. Creel [26] published the ^{11}B spectrum for ZrB_2 noting "*the unexplained doublet structure of the ^{11}B central line which is common to almost all the ^{11}B NMR spectra of the diborides*" and noting that the splitting was independent of field. Creel also observed the ZrB_2 first-order quadrupolar satellites, meaning that the anticipated values of second-order quadrupolar splitting of the central line, Δ, for $Zr^{11}B_2$ would be expected to be only ~40 Hz at 1.17 T, very much smaller than the observed doublet structure. Creel, with Torgeson and Barnes [70], later attributed this splitting to a Pake doublet [71]. The relationship for the dipolar coupling constant (ν_D) in Hz, for ^{11}B–^{11}B spin pairs in the graphite-like boron layer of the C32 AlB_2-type structure, is [31,70]:

$$\nu_D = \left(\frac{3}{2}\gamma\right)\left(\frac{3}{2}\gamma\right)\frac{\mu_0 h}{4\pi r^3} = \frac{9\gamma^2\mu_0 h}{16\pi r^3} \quad \text{(Eq. 2)}$$

where μ_0 is the vacuum permeability ($4\pi \times 10^{-7}$) in N/A^2, γ is the gyromagnetic ratio in Hz/T, h is Planck's constant in J/Hz, and r is the separation between nearest neighbour spin pairs in meters. The key point here is to know what the splitting is a measure of, in the system being studied. In some cases, the measured splitting is the dipolar coupling constant ν_D, and in other cases the measured splitting is $\frac{3}{2}\nu_D$, $2\nu_D$, or $3\nu_D$. In these diborides, the dipolar coupling results from the nearest neighbour ^{11}B–^{11}B spin pairs separated by r in the graphite-like layer. Torgeson et al. [70] showed that, given there are three identical spin pairs making up the contribution when averaged over the powder, the dominant splitting should be $3\nu_D$, with the $2\nu_D$ splitting also detectable. The internuclear B–B distances for these isomorphous metal diborides are known from X-ray measurements (see Table 2), therefore it can be expected that the values of $2\nu_D$ vary between 8 and 11 kHz, and the values for $3\nu_D$ vary between 12 and 17 kHz. In the AlB_2-type diborides other dipolar interactions such as between ^{11}B and ^{10}B and the metal nuclei with magnetic moment can complicate the analysis, but these interactions are much less significant, so it is taken that ^{11}B–^{11}B interactions dominate. In the case of CrB_2, it is likely that Malyuchov and Povitskii [24] and Silver and Kushida [25] observed a Pake doublet and not quadrupolar effects in the central line. Michioka et al. [72] have observed a doublet structure of the central peak in CrB_2 single crystal work and attributed it potentially to vacancies or a defect causing local alternating magnetization, as the magnitude of the CrB_2 splitting (36 kHz at 7.48 T) is too large to be due to either second-order quadrupolar interactions or a Pake doublet, and intrinsic paramagnetic vacancy defects, known to exist in some diborides, may cause splitting or line broadening of that magnitude [73]. Kopp and Barnes [29] reported splitting of the central peak for AlB_2 as 15.78 kHz at 0.33 T, which if this splitting is assumed to be $3\nu_D$ gives a B-B distance of 1.74 Å. Turner et al. [74] published an AlB_2 spectrum showing the central peak doublet with splitting of ~14.8 kHz at 7.05 T which if this splitting is assumed to be $3\nu_D$ gives a B-B distance of 1.78 Å. These values compare reasonably well with the B-B distance measured by XRD of 1.734 Å. Baek et al. [38] detected the $3\nu_D$ splitting in the central peak of ^{11}B NMR spectra in ^{11}B isotopically-enriched MgB_2 powder at 110 K and 7.2 T and also detected the $2\nu_D$ splitting at 0.814 T. Baek et al. [38] calculated the internuclear B–B distance from these Pake doublets for MgB_2 as 1.72 ± 0.08 Å. Strässle et al. [75] measured ^{11}B NMR spectra in a single crystal of MgB_2 at 81 K and 9 T, detecting the $3\nu_D$ splitting of the central peak as ~16.25 kHz which, using Eq. (2), gives an internuclear B–B distance for MgB_2 as 1.73 Å. Fig. 3(a) shows the central peak splitting for MgB_2 as 10.9 ± 0.2 kHz, which if this value is $2\nu_D$ gives a value of 1.72 Å in agreement with others. It should be noted that Bastow [40] and Carter and Swartz [30] attributed the ^{11}B central line splitting to boron in the probe (i.e. empty

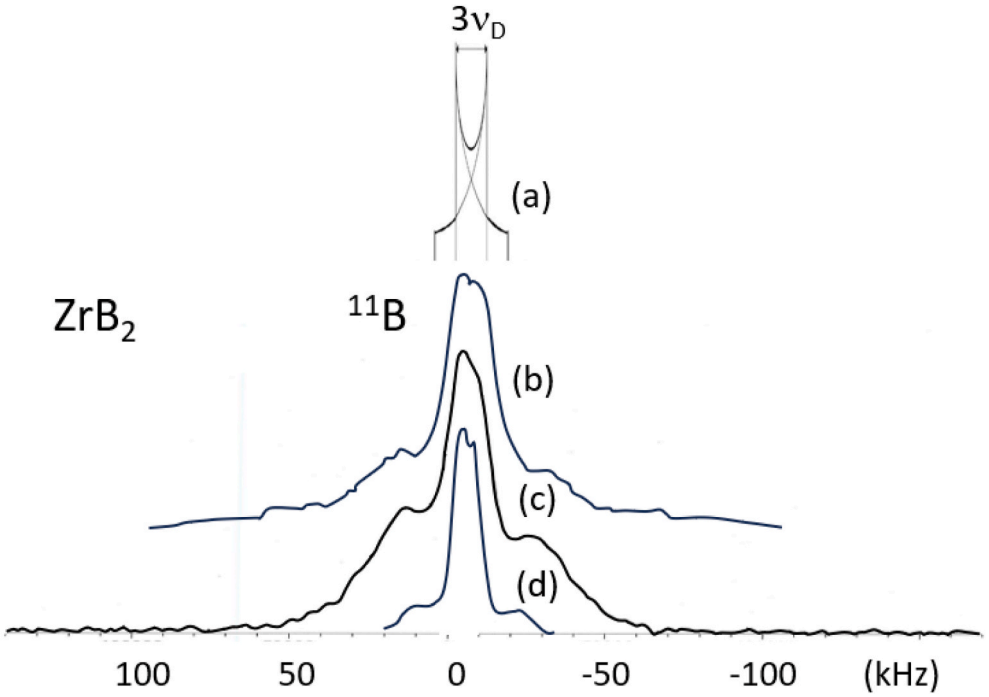

Fig. 4. (a) Dipolar Pake doublet schematic of the powder pattern produced by the direct dipolar interaction of one homonuclear spin pair in a static solid with splitting of 12.5 kHz equal to $3\nu_D$ such that r = 1.88 Å, and three ^{11}B spectra for ZrB_2 adapted from (b) Lue and Lai [44] at 9.4 T, (c) present work at 9.4 T, and (d) Creel [26] at 1.17 T showing the asymmetric doublet structure of the central peak.

coil signal). The ^{11}B empty coil background signal for the conditions used in the present work is not considered able to contribute to the observed asymmetry of the ^{11}B diboride central peak (Supplementary Fig. S12). Three independent ^{11}B NMR spectra of ZrB_2 showing the characteristic asymmetric central peak doublet attributed to the dipolar interaction of neighboring ^{11}B nuclei, are displayed in Fig. 4 along with a schematic Pake doublet of $3\nu_D = 12.5$ kHz for comparison. The ^{11}B data of Lue and Lai [44] obtained at 9.4 T show the asymmetric central peak with doublet structure for ZrB_2, HfB_2, and TaB_2 with the magnitude of the splitting increasing in that order (which agrees with the decreasing B-B distances from XRD). Fitting the splitting with a Pake doublet gives $3\nu_D$ values of 12.5 kHz, 14.8 kHz, and 15.6 kHz, such that r = 1.88 Å,

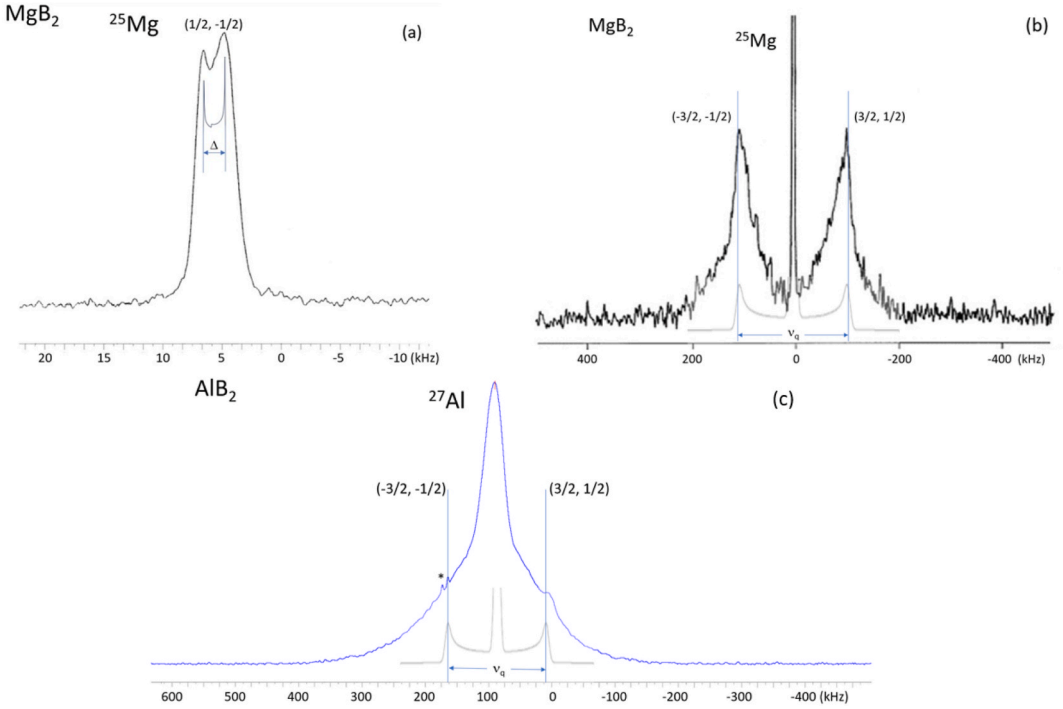

Fig. 5. ^{25}Mg NMR spectra for MgB_2 showing (a) central transition and (b) sharp first-order perturbed quadrupolar satellite splitting. Spectra in (b) are composed of two spectra with different offset frequencies exciting the satellites, with the central peak not fully excited. Adapted from Bastow [40], and (c) ^{27}Al NMR spectrum for AlB_2 showing central transition and weakly resolved first-order perturbed quadrupolar satellite splitting. Small sharp peak at 1680 ppm (marked with *) is due to elemental fcc Al impurity.

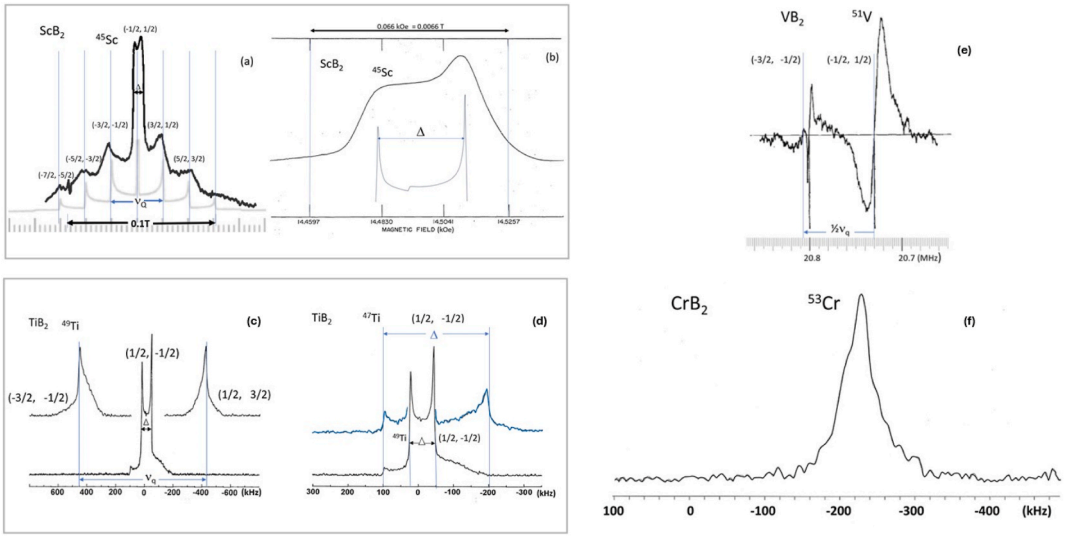

Fig. 6. (a) NMR spectrum adapted from Carter and Swartz [30] at 0.77T with central and satellite transitions for $^{45}ScB_2$. (b) NMR spectrum adapted from Creel [26] at 1.45T with central transition for $^{45}ScB_2$. (c) Three ^{49}Ti spectra taken at different offsets to capture the central (1/2, −1/2) transition and ±(1/2, 3/2) satellites for $^{49}TiB_2$. Satellites are shifted up on the y-axis to increase clarity. Note that the $^{49}TiB_2$ central transition is nested inside the $^{47}TiB_2$ central transition. (d) $^{47}TiB_2$ central transition shown shifted up on the y-axis with sharp second-order perturbed quadrupolar splitting Δ shown for $^{47}TiB_2$ (top spectra) and $^{49}TiB_2$ (bottom spectrum). Adapted from Bastow [42]. (e) The $^{51}VB_2$ spectrum adapted from the CW measurement of Silver and Kushida [25] over a 200 kHz spectral window exciting the (−3/2, −1/2) transition satellite 78 kHz away from the central (−1/2, 1/2) transition. (f) Static NMR data from CrB_2 showing the (1/2, −1/2) transition for ^{53}Cr.

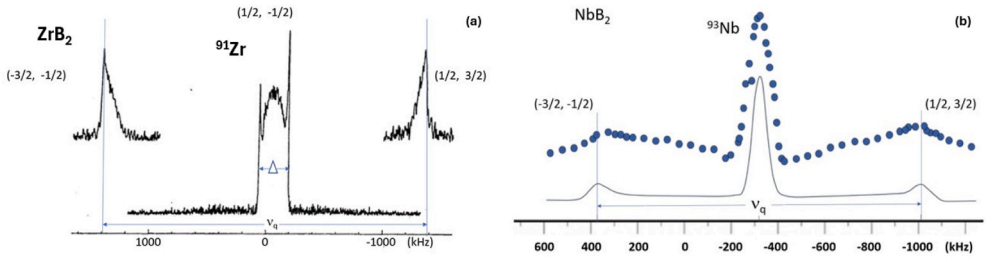

Fig. 7. (a) Three $^{91}ZrB_2$ NMR spectra taken at different offsets to capture the central (1/2, −1/2) transition and ±(3/2, 1/2) satellites. Satellites are shifted up on the y axis to increase clarity. (b) Static NMR data adapted from Su et al. [64] for NbB_2 showing the central transition and first-order perturbed quadrupolar satellite splitting ±(3/2, 1/2) for ^{93}Nb.

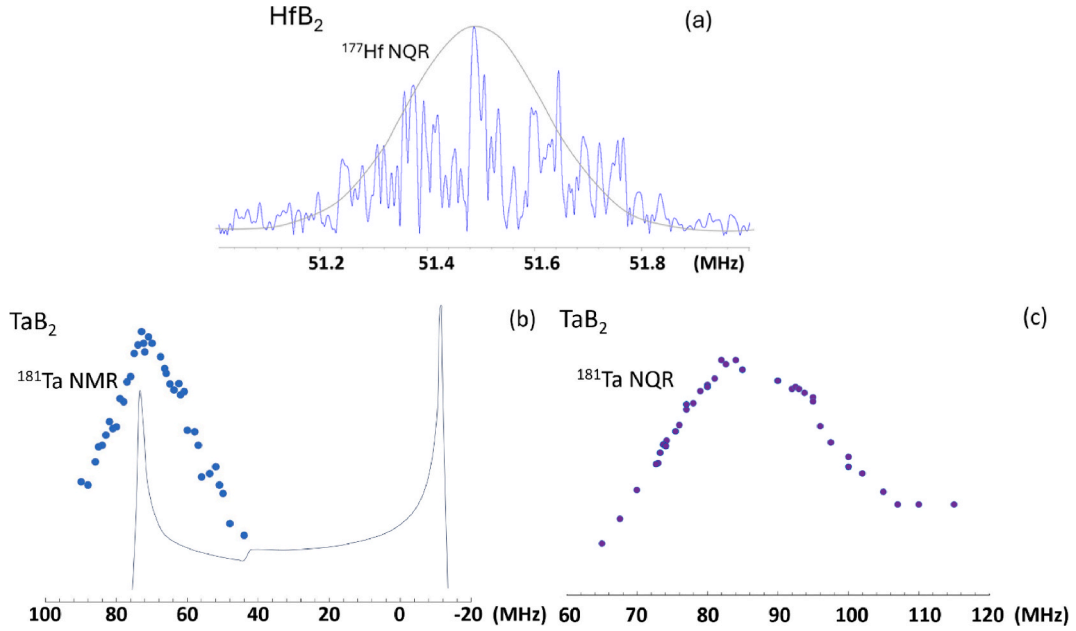

Fig. 8. (a) The $^{177}HfB_2$ (I = 7/2) NQR resonance in zero field at 51.5 MHz with Gaussian fit. (b) ^{181}Ta static NMR at 9.4T, broad peak centered at 70 MHz with simulated central line (1/2, −1/2) transition underneath. (c) ^{181}Ta zero field NQR at 295K with broad peak showing a center of gravity at 86.5 MHz.

1.78 Å, and 1.75 Å, for ZrB_2, HfB_2, and TaB_2 respectively. These r values are systematically larger than the B-B distances determined from crystallography, but with overall good agreement, especially for their relative values.

3.4. Knight shift measurements for ^{11}B site in the AlB_2 structure-type metal diborides

The values for the ^{11}B Knight shift, referenced to $NaBH_4$ in aqueous solution, are reported in Table 1 and further discussed in Sec. 3.5. It should be noted that different shift references have been used by different authors and therefore values need to be carefully examined and potentially re-referenced to allow comparison. For BF_3 used as the reference compound [38,41] a correction is +38.7 ppm, i.e. BF_3-OEt_2 is 0 ppm with respect to itself or −38.7 ppm with respect to aq $NaBH_4$ [89]. Some authors use aqueous triethyl borate $B(C_2H_5O)_3$ as the reference compound, with the resulting shift correction then +56.8 ppm with respect to aq $NaBH_4$ [89]. The ^{11}B Knight shift values reported in the present work compare reasonably well with previously reported values once the zero reference corrections are made and noting that typical uncertainty reported in the work of Barnes [28,29] is ±50 to ±100 ppm (Supplementary Table S13). One exception is the value for ^{11}B K_{iso} reported by Kopp and Barnes [29] in AlB_2 as −200 ± 50 ppm which is not in agreement with our value of +30 ± 10 ppm. Note also the IUPAC reference is different to that used by the solid-state NMR community. In this paper we have ensured through Table S9 that ready conversion of all the shift data to the IUPAC reference can be readily achieved.

3.5. NMR interactions at the metal sites in the AlB_2 structure-type metal diborides

The early CW NMR work on AlB_2 structure-type metal diborides predominantly concerned ^{11}B due to its combination of a relatively high Larmor frequency and relatively small quadrupolar interaction making it a more straightforward nucleus to study compared to many of the metal (M) nuclides available. Data in that early period were reported for ^{27}Al, ^{45}Sc, ^{51}V, and ^{89}Y [25,29,30,90,91], although the corresponding spectra were often absent. The nuclear properties of the other nuclei that can be potentially studied are given in Supplementary Table S5. Literature data and new measurements are presented here in Sec. 3.5 for each of the possible M nuclides in these isostructural AlB_2 compounds.

3.5.1. $^{25}MgB_2$ and $^{27}AlB_2$, main group metal diborides of the 3s Period

Sharp first-order and second-order quadrupolar perturbed ^{25}Mg NMR features of MgB_2 obtained at 9.4 T are shown in Fig. 5. The central transition singularities Fig. 5 (a) give a value of $\Delta = 2.39$ kHz and the second-order quadrupolar frequency $\nu_q(2) = 205.5 \pm 15$ kHz such that $C_q(2) = 1.37 \pm 0.1$ MHz. In Fig. 5 (b) the two ±(1/2, 3/2) satellites were

excited using two different pulses to delineate the sharp singularities. The singularities give $\nu_q(1) = 223 \pm 3$ kHz, leading to $C_q(1) = 1.49 \pm 0.02$ MHz. The central transition is not fully excited in Fig. 5 (b). The value of $C_q(2)$ is within 8% of the more accurate $C_q(1)$.

The ^{25}Mg K_{iso} measured from Fig. 5 (a and b) is 260 ± 10 ppm. When the first- and second-order derived quadrupolar frequencies are known, the axial component of the Knight shift can be calculated from [42,73,92].

$$K_{ax} = \frac{5\nu_q(1)\left[\pm\left[\nu_q(2) - \nu_q(1)\right]\right]}{\nu_L^2} \quad \text{(Eq. 3)}$$

where ν_L is the Larmor frequency, giving $K_{ax} = \pm 32 \pm 10$ ppm. This relatively small value compares reasonably well with the previously reported K_{ax} values of +50 ± 10 ppm [40] and +10 ppm [93].

Fig. 5 (c) shows the ^{27}Al NMR spectrum of AlB_2 at 9.4 T for a well crystallized high purity sample. The ^{27}Al peak is centered at 92 kHz (880 ppm) and can be fitted with two gaussians of FWHM 35.6 and 203 kHz. For the first-order broadened satellite transitions, the detailed features of the pattern are resolved at 166 kHz (1595 ppm) and 11 kHz (105 ppm). To the best of our knowledge this is the first published ^{27}Al NMR spectrum of AlB_2 identifying both first-order ±(3/2, 1/2) singularities. These singularities correspond to $\nu_q = 155$ kHz and $C_q = 1.03 \pm 0.01$ MHz. A peak at 175 kHz (1680 ppm) is from elemental Al impurity as confirmed by XRD (Supplementary Figure S3.1). Kopp and Barnes [29] did not publish their ^{27}Al spectrum for AlB_2, but they did report a broad weak component symmetrically underlying the central resonance and attributed the strongest point, located 72 ± 16 kHz from the central peak, to the (3/2, 1/2) satellite. This measurement of one satellite giving ½ν_q would then result in $\nu_q = 144 \pm 32$ kHz and $C_q = 0.96 \pm 0.2$ MHz, in good agreement with our $^{27}AlB_2$ data in Fig. 5 (c). However, it should be noted that Kopp and Barnes reported ν_q as 0.072 ± 0.016 MHz in their Table I [29]. It is thus believed the value for $C_q = 1.03 \pm 0.01$ MHz determined here from the two ±(3/2, 1/2) satellites is the most accurate to date.

The AlB_2 ^{27}Al Knight shift of +880 ± 40 ppm determined here is consistent with that reported by others [29,38,41]. There is some discussion in the literature regarding the correct ^{27}Al Knight shift of AlB_2 due in part to the broad underlying gaussian at 880 ppm as well as the inability of DFT methods to adequately predict the ^{27}Al Knight shift [35,38,94]. The accuracy of DFT Knight shift calculations is further discussed in Sec. 4.1 and 4.3. Ferriara et al. [94] suggest that the peak at 1680 ppm could be due to AlB_2. However, the peak at 1680 ppm can be unequivocally attributed to elemental aluminum based on both its coincidence with the well-known value of elemental fcc aluminium, and the percentage of the 1680 ppm peak, determined as 5 % being the level detected by XRD in this sample (Supplementary Figure S3.1). Corundum is also a minor impurity in this sample at 2 %, and α-alumina (Al_2O_3, corundum) has a well-known peak located at 14 ppm with a FWHM of 10 ppm which, if present, may show up in Fig. 5 (c) as a small peak at 1.5 kHz with a FWHM of 1 kHz, (a very sharp small peak). Such a peak would be less than half the intensity of the elemental Al peak at 1680 ppm and could have a relatively long relaxation time, so is not observed here. In summary with some confidence, the peak at 880 ppm (92 kHz) in Fig. 5 (c) is the central peak of AlB_2, with the ±(1/2, 3/2) singularities at 1595 ppm (166 kHz) and 105 ppm (11 kHz), and the peak at 1680 ppm (175 kHz) is attributed to the 5 % elemental Al impurity.

3.5.2. *$^{45}ScB_2$, $^{47,49}TiB_2$, $^{51}VB_2$, and $^{53}CrB_2$, transition metal diborides of the 3d Period*

Estimates for C_q of ^{45}Sc can be made for ScB_2 from both first- and second-order broadened spectral data of Carter and Swartz obtained at 0.77 T [30] and from Creel obtained at 1.45 T [26] as shown in Fig. 6 (a and b). The singularities of the satellite transitions are used to determine the first-order $C_q(1)$ value, and the central transition splitting, Δ, is used to determine the second-order $C_q(2)$ value. In Table 1 the C_q values stated have been redetermined here directly from the previously published spectra (Fig. 6 (a and b)). The CW NMR spectrum, data in Fig. 6 (a), shows a textbook example of the spectrum expected from a spin-7/2 nucleus with three pairs of satellites. Fig. 6 (b) shows the central transition measured by Creel [26] at 1.45 T. Carter and Swartz published values of 6.1 MHz and 6.2 MHz, respectively, for their first- and second-order determined C_q values, and the discrepancy is believed to lie in the value for the gyromagnetic ratio of the nucleus, γ, used by Carter and Swartz [30], which is corrected here. The analysis here suggests (Fig. 6 (a)) the most accurate $C_q(1) = 5.31 \pm 0.25$ MHz from the first-order splitting, and the value deduced from the second-order central line splitting Δ gives $C_q(2) = 5.82$ MHz. The second-order determined C_q value is within 10% of the more accurate first-order C_q value. From Fig. 6 (b), the second-order C_q value is determined as $C_q(2) = 5.81$ MHz indicating consistency of $C_q(2)$ values from two separate research groups on high quality samples of different origin.

The ^{45}Sc K_{iso} derived from Fig. 6 (b) is +900 ± 100 ppm. This value is within 20% of values reported by Barnes [28] of +600 ppm and Carter and Swartz [30] of +700 ± 100 ppm. When $\nu_q(1)$ and $\nu_q(2)$ are known, as above using Eq. (3), gives a relatively large $K_{ax} = \pm 1086$ ppm. Barnes et al. [28] report that ^{45}Sc Knight shift anisotropy (KSA) is negligible in ScB_2, but they did not publish a spectrum. Carter and Swartz [30] report no axial Knight shift pattern apparent from their spectrum reproduced in Fig. 6 (a).

Titanium has two NMR-active isotopes (^{47}Ti, ^{49}Ti) which have very similar magnetic moments, such that at 9.4 T they only differ in frequency by ~6 kHz. Fig. 6 (c) shows the satellite transitions ±(1/2, 3/2) for ^{49}Ti (I = 7/2) in TiB_2 as reported by Bastow et al. [42] with a separation, $\nu_q(1) = 882 \pm 2$ kHz, with $C_q = 42\nu_q/3$ then giving a first-order value for TiB_2 C_q (1) = 12.35 ± 0.02 MHz. The central transition (1/2, −1/2) splitting, Δ = 68.3 ± 5 kHz, is used in Eq. (1) to determine the second-order $\nu_q(2) = 770 \pm 30$ kHz and hence $C_q(2) = 10.78 \pm 0.42$ MHz for TiB_2. The $C_q(2)$ value is within 15% of the more accurate $C_q(1)$. The pulse used to excite the ^{49}Ti central transition also excites one of the ^{47}Ti (I = 5/2) singularities of the (1/2, −1/2) transition as shown in the lower spectrum of Fig. 6 (c). Both singularities of the ^{47}Ti central transition of TiB_2 can be excited using two pulses as shown in Fig. 6 (d), giving the TiB_2 ^{47}Ti central transition splitting Δ = 305.5 ± 15 kHz and $^{47}TiB_2$ $C_q(2) = 14.86 \pm 0.37$ MHz. Although a comparison of the ratio of first-order coupling constants should be more accurate, in this case we can determine the ratio of the $^{47}TiB_2$ second-order quadrupole coupling constant to the $^{49}TiB_2$ first-order quadrupole coupling constant and use that value to check the ratio for the 2018 Q values [33] for the two isotopes. The ratio ^{47}Ti $C_q(2)/^{49}$Ti $C_q(1) = 14.86/12.35 = 1.20$, while the ratio ^{47}Ti Q/^{49}Ti Q = 30.2/24.7 = 1.22, indicating satisfactory agreement.

The TiB_2 Knight shift for ^{49}Ti can be measured from Fig. 6 (c and d) as −400 ± 100 ppm. The Knight shift for the ^{47}Ti isotope is obscured by the ^{49}Ti central resonance in Fig. 6 (d); however, the Knight shift can be estimated at 9Δ/25 from the central resonance downfield singularity, where Δ = 305.5 kHz, such that the Knight shift is −440 ± 50 ppm, i.e. in good agreement. When $\nu_q(1)$ and $\nu_q(2)$ are known, as above using Eq. (3) gives a value of $K_{ax} = \pm 970$ ppm [42].

Silver and Kushida [25] first reported the ^{51}V resonance in VB_2 using CW NMR at a field of 1.84 T and $\nu_L = 20.66$ MHz producing the spectrum shown in Fig. 6 (e). The analysis method used at that time gave a value $C_q = 2.35 \pm 0.17$ MHz. Barnes et al. [91] also report the quadrupole coupling constant for VB_2 of ^{51}V as $C_q = 2.35$ MHz, but they did not present a spectrum. Our analysis of the Silver and Kushida spectrum in Fig. 6 (e) indicates $C_q = 2.18 \pm 0.2$ MHz, a value consistent with their value sitting at the lower end of their standard deviation range. The Knight shift reported by Silver and Kushida was −3370 ± 30 ppm based on the CW zero crossing at 20.73 MHz and their 1.84 T field consistent with their spectrum reproduced in Fig. 6 (e). This value is within 10% of values reported by Barnes et al. [91] of −3300 ppm and Castaing et al. [90] of −3000 ppm.

Bastow et al. [43] recently reported the ^{53}Cr resonance in CrB_2, locating the central resonance at a Knight shift of −9982 ppm using the frequency stepping method. In the present work, a two-pulse echo is successful in exciting the resonance, giving the narrowly peaked somewhat asymmetric lineshape, with $K_{iso} = -9990 \pm 70$ ppm, shown in Fig. 6 (f). Here, using the FWHM = 38 ± 8 kHz as the second-order quadrupolar perturbed central linewidth Δ (Eq. (1)) gives a value of $C_q(2) = 2.57 \pm 0.25$ MHz. Previous unsuccessful searches for the $^{53}CrB_2$ resonance had been attributed to "*the combination of low natural abundance, small gyromagnetic ratio, and strong quadrupole coupling of ^{53}Cr rendering its resonance undetectable*" in CrB_2 [95]. Rather than the $^{53}CrB_2$ resonance being difficult to detect, the Knight shift for $^{53}CrB_2$ was unexpectedly large and located far from the Knight shift for elemental chromium at +6870 ppm [43,96]. This point is further discussed in Sec. 4.1.

3.5.3. $^{89}YB_2$, $^{91}ZrB_2$, and $^{93}NbB_2$, transition metal diborides of the 4d Period

For completeness across this isostructural series the previously reported NMR data on ^{89}Y is recapped here. Barnes [28], and Carter and Swartz [30] measured ^{89}Y NMR, but did not publish the spectra. The YB_2 sample of Carter and Swartz contained a second phase whilst the sample of Barnes was "virtually single phase" [28]. As ^{89}Y (I = 1/2) is not a quadrupolar nucleus, a single symmetric resonance line is expected for YB_2. Barnes [28] reports the YB_2 Knight shift with respect to a saturated solution of YCl_3 as $K_{iso} = 1600 \pm 100$ ppm with no measurable K_{ax}, and Carter and Swartz [30] report $K_{iso} = 2000 \pm 300$ ppm in reasonable agreement.

Very sharp first-order and second-order quadrupolar perturbed ^{91}Zr NMR spectra are obtained at 9.4 T for ZrB_2 as shown in Fig. 7 (a). The satellite transitions ± (1/2, 3/2) and their separation determine $\nu_q(1) = 2.77 \pm 0.02$ MHz, with $C_q = 20\nu_q/3$ giving $C_q(1) = 18.47 \pm 0.1$ MHz. The central transition (1/2, −1/2) splitting, $\Delta = 244 \pm 20$ kHz, is used in Eq. (1) to determine $\nu_q(2) = 2.56 \pm 0.1$ MHz and $C_q(2) = 17.07 \pm 0.7$ MHz. The second-order $C_q(2)$ value is within 10% of the more accurate $C_q(1)$ value. The ^{91}Zr Knight shift $K_{iso} = -1472 \pm 100$ ppm. Again, using $\nu_q(2)$ and $\nu_q(1)$ in Eq. (3) for I = 5/2 gives a relatively large value for $K_{ax} = \pm 2084$ ppm.

Su et al. [64] reported ^{93}Nb NMR spectra at 7.05 T (Larmor frequency 73.67 MHz) for high purity NbB_2 powder. Fig. 7 (b) shows the data adapted from Su et al. with the ±(3/2, 1/2) satellites giving $\nu_q(1) = 1.4 \pm 0.03$ MHz and $C_q(1) = 33.6 \pm 0.6$ MHz. Kotegawa et al. [97] performed ^{93}Nb NQR on NbB_2 finding a ±(7/2, 9/2) resonance at 6 MHz, which indicates $C_q = 36$ MHz, which is 7% larger than the NMR value for C_q. Kotegawa et al. [97] did not give the provenance of their NbB_2 sample nor did they show the NQR spectrum. The accuracy of C_q increases in this order: central transition singularities to give Δ, separation of satellite singularities to give ν_q, center of gravity of zero field NQR satellite transition resonance [59]. Given that the NQR spectrum is not documented, the NMR value of C_q from the satellite singularities will be taken as the most accurate value currently available. The isotropic Knight shift can be estimated from Fig. 7 (b) as −4300 ± 400 ppm which corresponds with the value −3900 ppm given by Su [64].

3.5.4. $^{177}HfB_2$ and $^{181}TaB_2$, transition metal diborides of 5d Period

An attempt to locate the ^{177}Hf NQR signal in HfB_2 was made over the frequency range 49 to 60 MHz. A weak echo was detected at 51.5 MHz as shown in Fig. 8 (a). Assuming the resonance at 51.5 MHz is the $^{177}HfB_2$ ±(3/2, 1/2) peak, then using $\nu_1 = \frac{2C_q}{28} = 51.5 \pm 0.5$ MHz, gives $C_q = 721 \pm 7$ MHz. To the best of our knowledge, no one has previously reported $^{177}HfB_2$ NQR measurements of C_q. Snyder et al. [98] measured C_q using $^{178}HfB_2$ Mössbauer spectroscopy resulting in $C_q = 717.6$ MHz. Using ^{181}Ta as a time-differential perturbed angular correlation spectroscopy (TDPAC) probe in HfB_2, Kaufmann [99] measured $C_q = 730 \pm 5$ MHz at 295 K and 719 ± 10 MHz at 4.2 K, with Haas and Shirley [100] determining $C_q = 720 \pm 19$ MHz at 295 K. The similarity of these values supports the assignment of the weak NQR resonance at 51.5 MHz to the $^{177}HfB_2$ ±(3/2, 1/2) singularity. Given that these are NQR measurements no comment can be made about the Knight shift for hafnium from Fig. 8 (a). As discussed in Sec. 4.1, using the entire data set for this isomorphous series and the K_{iso} values for the pure parent metals reveals systematic trends allowing an estimate of the $^{177}HfB_2$ $K_{iso} = -2357 \pm 300$ ppm.

In a 1974 study by Creel et al. [101] of the related monoborides, no tantalum resonance could be observed for TaB. The very large quadrupole moment of ^{181}Ta, and therefore large quadrupole interaction (~500 times greater than ^{27}Al for the same structural distortion), makes it difficult to observe by NMR, even more so under the conditions of the 1974 study. In the present work, the large linewidth was excited by stepping through the frequency range point by point. The Larmor frequency, ν_L, for ^{181}Ta at 9.4 T is 48.52 MHz, so the static high field NMR powder pattern was searched for over a ~45 MHz spectral window from 44 to 90 MHz. A broad resonance with centre of gravity at 70 MHz was

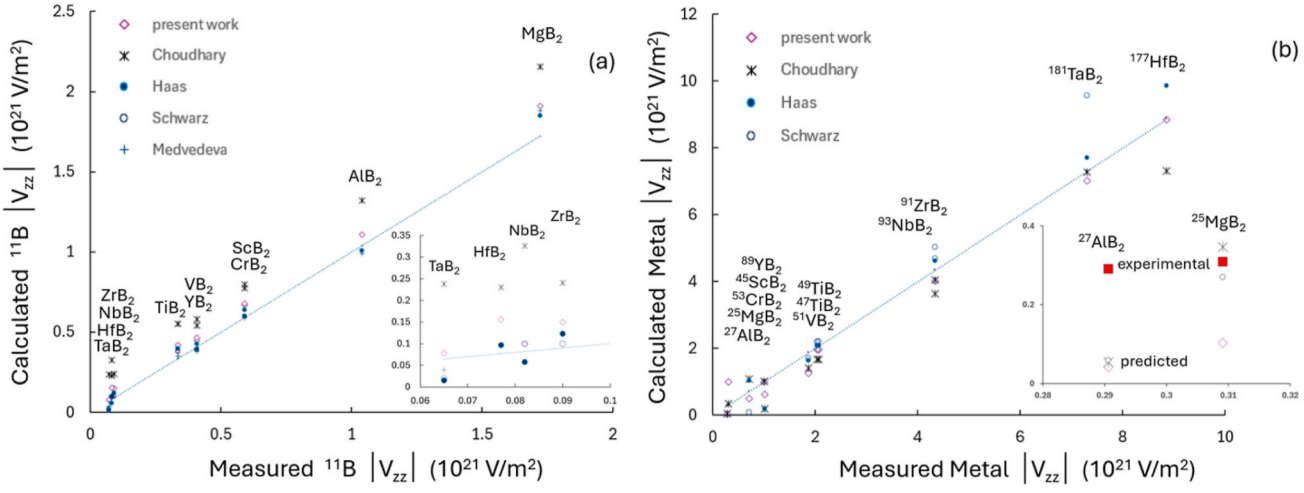

Fig. 9. Comparison of calculated and measured V_{zz} values for (a) boron sites and (b) metal sites, from data in Table 1. Measured values fall on the dotted lines. Calculated values are shown as symbols. The calculated values of the present work ◊ are compared to calculated values reported by others [39,69,103,104] with all values tabulated in Supplementary Table S7. Inset for the boron site V_{zz} values highlights the range of predicted values for the diborides with measured experimental ^{11}B $|V_{zz}| < 0.1 \times 10^{21}$ V/m^2. Inset for the metal site V_{zz} values highlights the discrepancy between $^{27}AlB_2$ and $^{25}MgB_2$ predicted and measured experimental values.

observed as shown in Fig. 8 (b). If the broad NMR peak is modelled as part of the static second-order powder pattern of the central transition [31], then 9Δ/25 ≈ (75 - 44) MHz and Δ ≈ 86.1 MHz, such that $\nu_q \approx 40.0 \pm 0.4$ MHz and $C_q \approx 560 \pm 5$ MHz. The starting point for the NQR frequency search at room temperature for ^{181}Ta is determined by the three NQR frequencies calculated from the above preliminary estimate of the C_q value ≈ 560 MHz. This frequency for ±(1/2, 3/2) is $\nu_1 = \frac{2C_q}{28} =$ 40 MHz, and then multiples of two and three times this for the other transitions. A spectral window of 45 MHz was searched for zero field NQR resonance, starting at 65 MHz based on the tuning range of one Bruker plug-in for the Bruker 400 Avance console. A broad resonance with centre of gravity at 86.5 MHz was observed as shown in Fig. 8 (c). Given the very broad frequency range examined in the NQR and variations in tuning and the power output of the transmitter over such a range, the centre of gravity of the broad peak structure is taken as the (−5/2, −3/2) satellite giving $\frac{4C_q}{28} = 86.5$ MHz, yielding $C_q = 605.5$ MHz. There is good consistency between these different experimental measurements, with the value from NQR within 10% of the value from NMR. To the best of our knowledge, we believe this to be the first report of ^{181}Ta NMR and NQR measurements in TaB_2 to determine C_q.

Given the width of the resonance in Fig. 8 (b) there is little that can be definitively said about the Knight shift in $^{181}TaB_2$ although it is likely to be large and negative. As discussed in Sec. 4.1, using the systematic trends in our entire data set, we can interpolate an estimate of the $^{181}TaB_2$ $K_{iso} = -5574 \pm 400$ ppm.

3.6. Comparison of experimental and calculated quadrupolar interactions

As mentioned in Sec. 2.4, the EFG tensor, including its magnitude and sign, is calculated using quantum mechanics whilst experimental NMR measures the magnitude of C_q and hence the absolute value of the EFG. Several approaches to DFT calculation of quadrupolar interaction parameters have been reported based on electronic structure methods that use a local density approximation (e.g. LDA, GGA, etc.) to describe the wave function near the nucleus, including linearised augmented plane wave (LAPW) codes such as WIEN2k [34] and CASTEP [102] where relativistic effects can be included, such as the zeroth order regular approximation (ZORA). The DFT calculated results of the present work are shown in Table 1, and the EFG values are compared in Fig. 9 (Supplementary Table S7 and S17) to values from past theoretical studies [39,69,103,104]. Examination of all past calculated values indicates that calculations can be within 10% of measured values for ten of the eleven metal diborides studied, but not systematically accurate for any single DFT approach. The issue of extremely poor accuracy with EFG calculations for $^{27}AlB_2$ is discussed further below. The ^{11}B EFG and therefore C_q values calculated here are consistently at least 10% higher than those measured, due presumably to systematic errors in the CASTEP DFT-based calculation, and in the cases of ^{11}B in TiB_2, ZrB_2 and HfB_2, the CASTEP DFT values calculated in the present work are 20-50% higher than the experimental values. However, ^{11}B V_{zz} values calculated using the WIEN package [39,69,105] fall within 10-15% of the experimental values for these three diborides. Noting that these three metals are Group IV where the bonding d states are full and at low density of states for 3d, 4d, and 5d transition metal diborides [9,10,12,37,106,107], this result should allow further refinement of the CASTEP-based DFT approach used for the ^{11}B EFG calculation. For the metal sites, comparisons between experimental and theoretical EFG values can show good agreement within ~5%. However, there are exceptions of $^{51}VB_2$ and $^{53}CrB_2$ (both are 3d metals) where the CASTEP calculation is within 30% and the WIEN calculations are within 5-15%. There is the exception of $^{25}MgB_2$ where the CASTEP calculation is 3 times too high, yet the WIEN calculation is within 15%. And the most notable exception is $^{27}AlB_2$ where the calculated and measured values differ by a factor of 3 to 7 when compared with all available DFT calculations.

The calculation of accurate EFGs is the subject of much research and has recently been reviewed [104]. For the CASTEP-based DFT method employed here, the worst agreement is for V_{zz} (and hence C_q) for the metal sites in the main group metal diborides $^{25}MgB_2$ and $^{27}AlB_2$ as shown in the inset of Fig. 9 (b). For $^{27}MgB_2$ our calculated V_{zz} value is -0.99×10^{21} V/m^2 and, by comparison, the calculated values reported in the literature range from -0.10 to -0.55×10^{21} V/m^2 [39,104,108] with the experimental result from NMR being $|V_{zz}| = 0.39 \times 10^{21}$ V/m^2. The one calculated V_{zz} for $^{25}MgB_2$ that is within 15% of the measured value [104] uses the VASP package, however this agreement is not consistent across the entire data set. For example, this VASP-based approach yields a calculated metal site V_{zz} value for another main group metal diboride, AlB_2, 80% different to the NMR measured value for $^{27}AlB_2$. As shown in Fig. 5 (c) and the inset of Fig. 9 (b), the present work has successfully measured both ±(3/2, 1/2) satellites to give the most accurate first-order C_q value from $^{27}AlB_2$ NMR experiments, which gives $|V_{zz}| = 0.29 \times 10^{21}$ V/m^2, and this experimental value is five to seven times larger than the calculated values for $^{27}AlB_2$ that range from -0.04 to 0.06×10^{21} V/m^2. The choice of the computational method—including the way that electrons are treated as relativistic objects—allows reliable prediction of the EFG tensors reflecting the chemical and structural environment of the nuclei. Typically, the calculated EFG parameters either systematically overestimate or underestimate the experimental ones due to errors in a DFT approximation [65]. The orbital character of the electrons dominating the EFG can provide valuable information about chemical bonding [109]. No single theoretical approach examined here gives the most accurate predictions across the entire set of diborides. These results are discussed further in Sec. 4.3.2.

4. Discussion

As acknowledged by the early theorists calculating bonding parameters and electronic structure for these AlB_2-structure type diborides [9,10,37,51,110], it is important to recognise trends in bonding across the Groups and Periods of related compounds to gain a qualitative understanding of the property variation. In Sec. 4.1, the experimental Knight shift values from Table 1 are compared to density of states and d-band center calculations at 0 K, and electronic specific heat coefficient values measured at low temperature as given in Table 2. The contributions to K_{iso} from the electron orbital effects (Fermi surface electrons) and the spin contribution (core polarization or Fermi contact interaction effects) can be understood through such comparisons, and where possible K_{iso} values can be calculated *ab initio* to further confirm the dominant contributions. In Sec. 4.2 the experimental C_q and V_{zz} results from Table 1 are presented and compared to experimental and calculated cohesive properties given in Table 2. The electron and lattice contributions to the EFG at the nucleus can be calculated *ab initio* to determine the dominant contribution, and Sec. 4.3 summarises the current state of the literature regarding the calculation of NMR parameters for comparison with experiment.

4.1. Knight shift relationship to electronic properties

Tabulation of the current 'best' experimental values for metal site Knight shift at room temperature for this isomorphous series allows missing data to be interpolated. The Knight shift data in Table 1 include two values, for $^{177}HfB_2$ and $^{181}TaB_2$, derived from the best fit linear regression relationship between K_{iso} values of the diboride metal site and pure metal, which yields: $|K_{iso(pure\ metal)}| = 1.9734|K_{iso(diboride)}|$ with correlation coefficient $R^2 = 0.93$, where the absolute values of K_{iso} are used, noting that all pure metal Knight shifts are positive for this series as are the metal site K_{iso} values for Group II and III diborides. The ^{177}Hf pure metal K_{iso} has not been measured, however a plot of the available pure metal K_{iso} values as a function of electron configuration for this set of critical metals gives a predicted value of ^{177}Hf $K_{iso} = 5072 \pm 300$ ppm for pure hafnium metal as shown in Supplementary Fig. S18. The

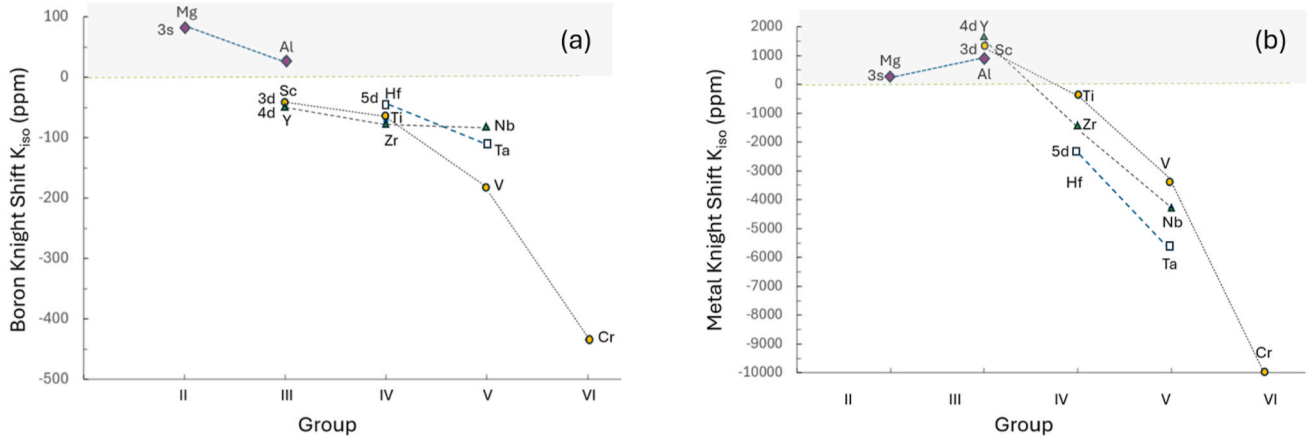

Fig. 10. Knight shift data for AlB_2-structure type diborides as a function Group and 3s, 3d, 4d, 5d Periods (a) for the boron site and (b) for the metal site.

$^{181}TaB_2$ Knight shift value appears to be negative from our NMR data. The $^{177}HfB_2$ Knight shift is assumed to be negative because the other Group IV, V, and VI transition metal diborides in this series have negative Knight shifts at the metal site. The K_{iso} data for the boron and metal sites are shown as functions of Group and Period in Fig. 10 (a and b).

All trends in K_{iso} are monotonic in the Period, transitioning from positive to negative at Group III as shown in Fig. 10. All K_{iso} values for the diborides become more negative in magnitude as the valence electron concentration increases within the Period, apart from the metal Knight shift data of the main group metals of Period 3s. The ^{11}B K_{iso} values range from +81 ppm for MgB_2 to −434 ppm for CrB_2. Baek et al. [38] calculate the ^{11}B and metal site Knight shifts for the main group metal diborides, MgB_2 and AlB_2, using both *ab initio* and numerical methods, noting that for AlB_2 the local density approximation (LDA) tends to overestimate the Fermi contact term. These calculations suggest that the Fermi contact interaction (core polarization) dominates the K_{iso} values for AlB_2 (^{27}Al and ^{11}B) and MgB_2 (^{25}Mg), with p-orbital effects dominating the ^{11}B Knight shift in MgB_2 [41]. The early work by several authors [25,26,30] discussed the interactions between the metal and boron layers in the transition metal diborides. Based on early band theory calculations for CrB_2, Liu et al. [48] suggested that core polarization would not effectively produce a Knight shift at the B nucleus in these diborides. For the transition metals of Periods 3d, 4d, and 5d, the metal donates electrons to the boron, with the K_{iso} data of Fig. 10 suggesting that the dominant residual contribution to the Knight shift values at both the boron and metal sites is due to d-electrons. The metal d-electrons are contributed to the d-band and reflected at the boron site due to core polarization, i.e. the Fermi-contact interaction of metal d-band and core electrons. The changes of the Knight shift at the boron site are commensurate with the changes in the d-electron susceptibility at the metal site, as indicated by the metal Knight shift data. These trends indicate that the underlying source of the Knight shift at both the metal and boron nuclei is this susceptibility. The data of Fig. 10 and the calculations of Baek et al. [38] support a dominant contribution to the ^{11}B K_{iso} from core polarization as a function of metal Group and Period for all except MgB_2. The metal site Knight shift data in Fig. 10 (b) also support the dominant contribution from core polarization. For the diborides where an axial Knight shift at the metal site could be evaluated (MgB_2, ScB_2, TiB_2, ZrB_2), the values of K_{ax} are similar in magnitude and sign to K_{iso}, suggesting similarity between the level of core polarization as indicated by K_{iso} and the progressive admixture of anisotropic d-like (MgB_2) or d orbitals into the conduction band wave function [42].

Blumberg et al. [111] noted that for the pure transition metals the magnitude of the K_{iso} value should get larger as the Period increases because the hyperfine interaction increases with atomic number. Comparison of K_{iso} values for the pure metals and the corresponding metal diborides is given in Fig. 11 from data available in Supplementary Table S13 and Fig. S18.

Using the data in Fig. 11, the K_{iso} ratio, $|K_{iso(diboride)}/K_{iso(pure\ metal)}|$, is shown to vary between 0.15 and 0.64 for all metals except Cr which stands out in this series as having the only K_{iso} ratio >1 at 1.45. This exception underscores the surprise expressed by Bastow [43] in first detecting the $^{53}CrB_2$ resonance at −9982 ppm. Fig. 12 (a and b), compiled from data in Table 2, shows that CrB_2 also has the largest DOS and electronic specific heat values for this set of diborides. Examination of the electronic specific heat coefficient ratio for the diborides and pure metals shows that $\gamma_{(diboride)}/\gamma_{(pure\ metal)}$ for this series varies between 0.21 and 0.53 for all metals except Cr which stands out in this series as having the only γ ratio >1 at 8.77 as shown in Supplementary Table S16, suggesting that itinerant antiferromagnetism, both in pure Cr metal with $T_N = 313$ K and in CrB_2 below $T_N = 88$ K, affects the values of electronic specific heat coefficient [50,112]. The room temperature K_{iso} values, which are dominated by the Fermi contact interaction for the diborides, do not correlate with the low temperature electronic specific heat coefficient values for the diborides.

The electronic specific heat coefficient, γ, values for the diborides are proportional to the total density of states at the Fermi level, $N(E_F)$, as indicated by the free electron model [113]:

$$\gamma = \frac{\pi^2}{3} k_B^2 N(E_F) \qquad \text{(Eq. 4)}$$

A comparison of the data in Table 2 with Eq. (4) indicates proportionality ($R^2 = 0.97$) with the coefficient of proportionality, $\frac{\pi^2}{3} k_B^2$ where k_B is Boltzmann's constant, being 15% lower than the best fit linear regression value for the data compiled in Table 2, which seems to be in reasonable agreement (see Supplementary Fig. S16). One compound, CrB_2, lies well outside the γ and total DOS values for the other diborides (by a factor of 2.8 to 4 times larger than VB_2) as shown on the secondary y-axes in Fig. 12 (a and b). The CrB_2 compound has the largest values of the entire data set, a trend reminiscent of the K_{iso} values where CrB_2 values are 2.4 to 3 times greater than the values of VB_2, as discussed above. There is an inflection point at Group IV for the electronic properties in Fig. 12 (a and b). As noted by Carter [10] and others [9,37,47,54], the bonding d states are filling for 3d, 4d, and 5d Periods up to Group IV, followed by filling of the antibonding d states from Group IV to V and VI. The DOS and γ values reflect the bonding states to antibonding states transition as an inflection point at Group IV, however the Knight shift values do not. It is well known that when the experimental Knight shift values are not described by the free electron model for the DOS, that the Knight shift can help elucidate the formation of chemical bonds and the hybridization of orbitals [106]. As the K_{iso} values are not proportional to the DOS or γ values, the results suggest that the conduction electrons are involved in the electron sharing or covalent

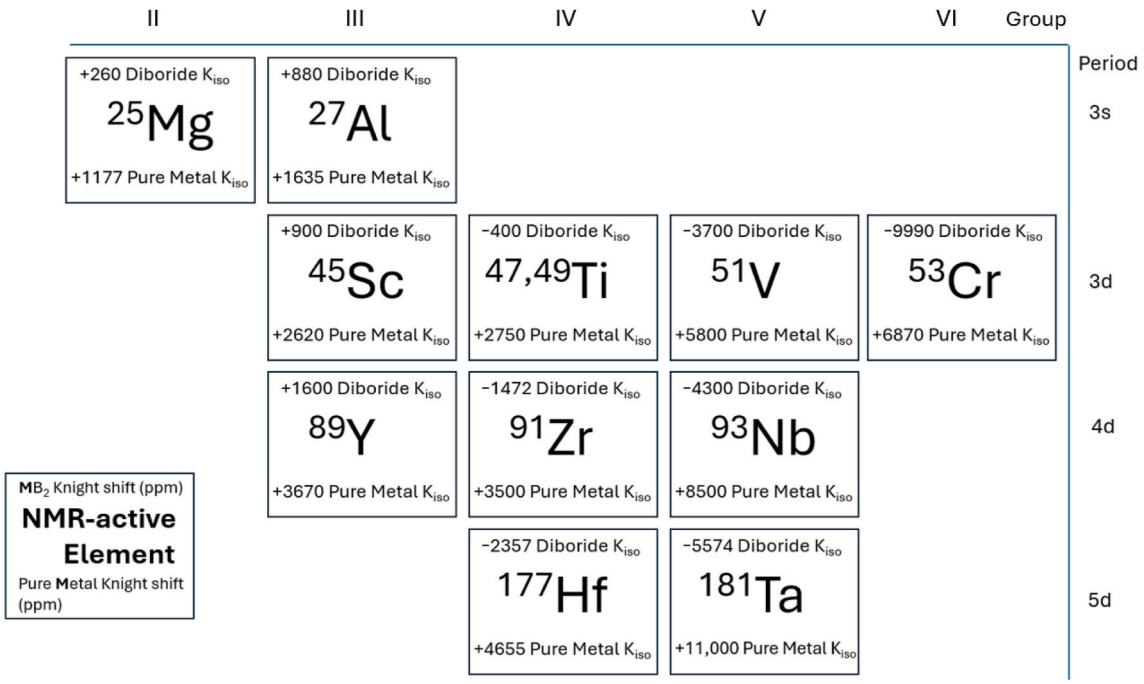

Fig. 11. Periodic Table with NMR K_{iso} values for the metal sites in the diborides as compared to the pure metal. The ^{177}Hf K_{iso} values and the ^{181}Ta diboride K_{iso} value are interpolated from the experimental data available in Supplementary Table S13 and Fig. S18.

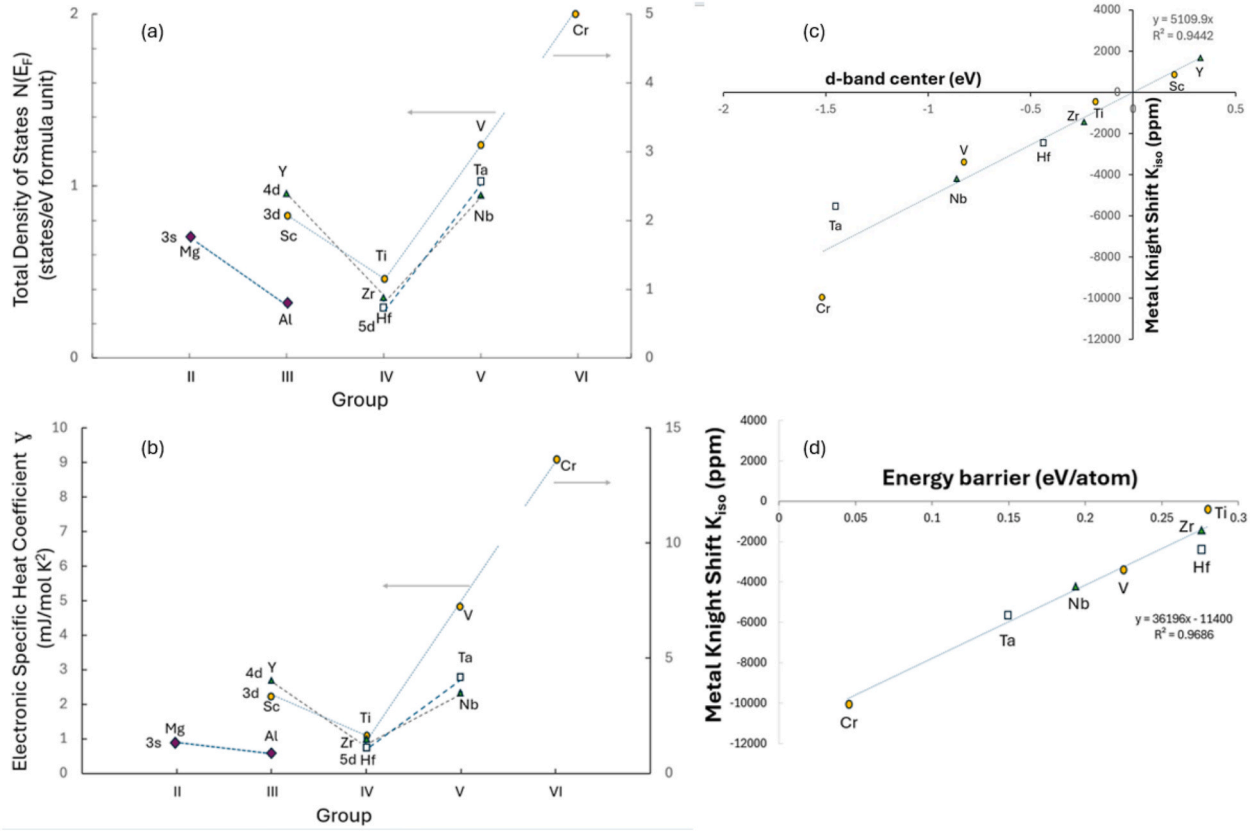

Fig. 12. (a) Total density of states and (b) electronic specific heat data compiled from the literature for this set of isomorphous diborides. CrB_2 values are shown on the secondary y-axes. (c) Relationship between K_{iso} values at the metal site and d-band center values for the transition metal diborides. (d) Relationship between K_{iso} values at the metal site and the energy barrier to stacking transformation for seven of the transition metal diborides, using energy barrier data from Leiner et al. [114]. All other data from Table 2.

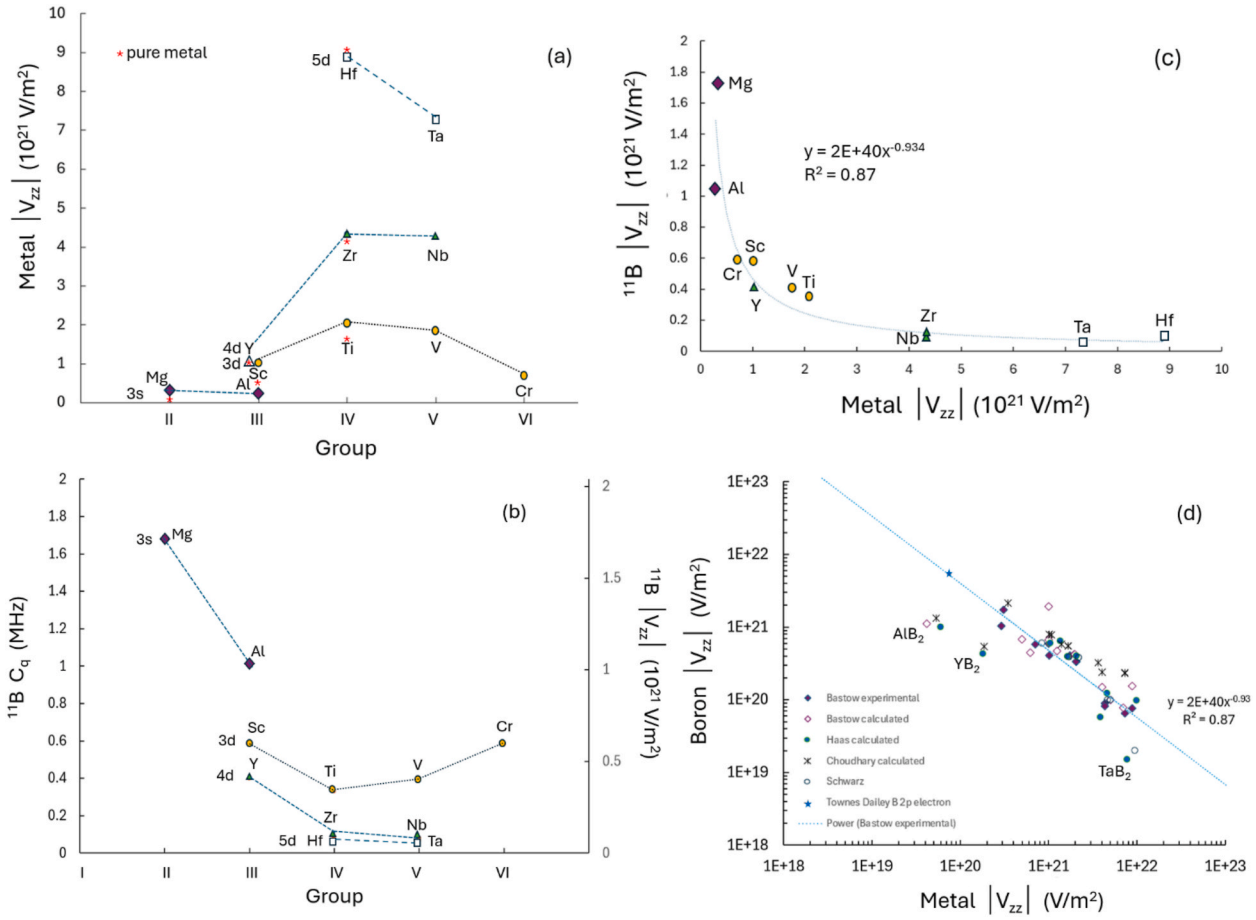

Fig. 13. Experimental results from NMR measurements of metal diborides plotted as functions of the parent metal Period and Group in the Periodic Table: (a) Metal site. The metal V_{zz} values for the diborides are compared with experimental values for the pure hexagonal metals (asterisk), (data from Supplementary Table S14). The open triangle for the metal site EFG in YB_2 is calculated based on trends in experimental data as described in the text. (b) Boron site V_{zz} values for the diborides. (c) Power law relationship between experimental values for metal site V_{zz} and ^{11}B V_{zz} for these isomorphous metal diborides. (d) Power law relationship between experimental V_{zz} values as compared to calculated values for metal site V_{zz} and ^{11}B V_{zz} for these isomorphous metal diborides (data from Supplementary Table S7). The extreme case for pure planar B-B bonding using the Townes Dailey approximation is shown as a solid star [23]. Calculated values greater than two standard deviations away from experimental best fit power law relationship are notated for AlB_2, YB_2, and TaB_2.

bonding, i.e. the hybridized metal d-like or d-states and boron p-states. Access to the room temperature Knight shift values for the entire series gives further insights into the electronic properties of these diborides and the importance of the d-band and d-like states as shown in Fig. 12 (c and d).

The metal site K_{iso} values for the transition metal diborides correlate well with calculated d-band center values (d-band center distance to E_F in eV) [15,87] as shown in Fig. 12 (c). Li et al. [15] have shown that the calculated d-band center acts as a descriptor of experimental catalytic activity for these diborides when in the form of nanoparticles with BET surface areas of 10-50 m^2/g. It is the electronic structure at the surface of the nanoparticles that determines the catalytic activity. Therefore, it seems likely that the K_{iso} values measured here in bulk metal diboride powders (325-mesh, <45 μm) are commensurate with those for nanoparticles and potentially 2D MBene nanosheets due to the layered nature of the AlB_2 structure (Fig. 1). Interestingly, Leiner et al. [114] have calculated a measure of layer stability based on the theoretical energy needed to overcome the barrier to alter stacking in AlB_2-type metal diborides, for example the change in layer stacking needed along a plane-by-plane transformation pathway from SG 191 *P6/mmm* to SG 194 $P6_3/mmc$, for seven of these diborides, and the energy barriers also rank in the order of the K_{iso} values as shown in Fig. 12 (d). The energy barrier is related to the layer stability as determined by the balance of occupation of bonding and antibonding states of these compounds. The relationships in Fig. 12 (c and d) suggest the utility of the metal site K_{iso} value in these diborides as a proxy for the bonding and antibonding d-band weighted average (the d-band center) and the energy needed to alter the stacking of the metal plane (energy barrier), respectively, both of which play a crucial role in bonding and stability, with TaB_2 and CrB_2 being at the high activity, low barrier end of these two related electronic parameters. The relationships also suggest that the core polarization effects, which dominate the metal site K_{iso} values, are critical to the catalytic activity and stability. In addition, the data in Fig. 12 (c) can be extended to estimate the center of d-like states in MgB_2 and AlB_2 [115, 116], based on the K_{iso} values, giving an estimate of d-band center values of 0.05 eV and 0.17 eV for MgB_2 and AlB_2, respectively. These results make a valuable connection between the metal site Knight shift and the catalytic performance of a wider range of compounds spanning the main group metals. Such a relationship has rich applications in the future development of material property descriptors from these NMR data, potentially useful in predicting materials that can overcome structure-property trade-offs such as catalytic activity and stability in both basic and acidic electrolytes. It is also possible that the metal site K_{iso} could be useful as a sensor for strain, doping, and defect engineering of the d-band center in MBenes, and such an investigation is suggested as potentially fruitful future work.

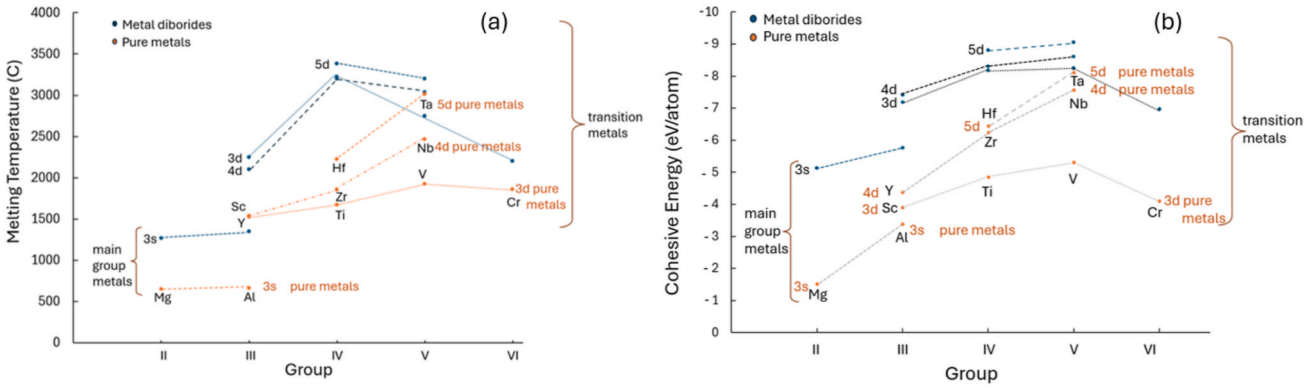

Fig. 14. (a) Melting point temperature data for diborides and pure parent metals. (b) Calculated cohesive energy values for diborides and pure parent metals.

4.2. Electric field gradient and nuclear quadrupole coupling constant relationship to bonding and cohesive properties

The measured quadrupolar data (C_q and V_{zz} for metal site and boron sites) systematically partition into separate families based on the 3s, 3d, 4d, 5d Periods as a function of Group as shown in Fig. 13 (a and b). The metal site V_{zz} and ^{11}B V_{zz} values follow a power law relationship as shown in Fig. 13 (c and d). For the pure parent metals with hexagonal close packed (hcp) hP2 structure (Mg, Sc, Y, Ti, Zr, Hf), the V_{zz} values have been previously reported, and we can now correlate these pure metal EFG values with the metal diboride values for this subset of the isomorphous series (see Supplementary Table S14 and Fig. S14). The measured metal EFG values are linearly related, with the V_{zz} of the pure hcp metal being 98% of the V_{zz} at the metal site in the hcp hP3 structure of the diboride. The effect of the boron layer on the metal site V_{zz} is the greatest in $^{25}MgB_2$ and then decreases with higher atomic number. Indeed, close examination of the metal site V_{zz} data, when compared to the hcp pure parent metal V_{zz}, shows that the M-M interaction has a systematically dominating effect with higher atomic number in this subset ($^{25}MgB_2$, $^{45}ScB_2$, $^{47,49}TiB_2$, $^{89}YB_2$, $^{91}ZrB_2$, $^{177}HfB_2$) of the series. This direct experimental measure of the effect of the boron layer on the metal site V_{zz} is available only for the diborides whose parent metals have hexagonal close packed structure.

Although ^{89}Y is spin ½ and has no quadrupole moment, Barnes et al. [117] used ^{45}Sc as a probe in solid solutions of Sc-Y showing that C_q increases monotonically with Y content, and the extrapolated value for pure Y metal is $C_q = 5.20$ MHz which gives $V_{zz} = 0.99 \pm 0.05 \times 10^{21}$ V/m^2 for elemental yttrium metal (see Supplementary Fig. S14). Using the correlation $|V_{zz(\text{pure metal})}| = 0.9785|V_{zz(\text{diboride})}|$, $R^2 = 0.99$, and the extrapolated value of EFG for elemental Y [117] allows calculation of the YB_2 EFG at the Y nucleus as $1.01 \pm 0.05 \times 10^{21}$ V/m^2 (see Supplementary Fig. S14). This interpolated value of EFG for the metal site in YB_2 is shown as an open triangle in Fig. 13 (a). The trends in NMR parameters are non-monotonic for Period 3d for the metal and boron sites and for Period 4d for the metal site V_{zz} values, where more than two compounds are measured in the Period, showing an inflection at Group IV.

4.2.1. Electron transfer from the metal to the boron

The theories of bonding for these diborides are encompassed by two extreme cases. The early discussion centered on these two extreme cases for bonding where either the boron network dominates the properties due to strong directional B-B bonding with supplemental strengthening from the metal atoms or the hexagonal M-M metal bonding dominates the properties with the boron atoms acting to strengthen the metals. In terms of the contributions from NMR to the early bonding picture, Silver [22] articulated the two extreme cases for the electron contribution to the EFG, and hence quadrupole coupling constant C_q, in AlB_2-type metal diborides as (1) the case of pure planar B-B bonding without metal atom bonding or interplanar bonding (i.e. 2D graphite-like sheets of boron), with an ^{11}B EFG calculated from the Townes Dailey approximation [118] as $|V_{zz}| = 5.49 \times 10^{21}$ V/m^2 and $C_q = 5.39$ MHz, and (2) the case where the metal atom contributes two electrons to create a spherically symmetric electron configuration at the boron nucleus with the ^{11}B $V_{zz} = 0$ and hence $C_q = 0$. Examination of Table 1 and Fig. 13 (b) indicates that MgB_2 is the most like case 1 (even though the $Mg^{11}B_2$ V_{zz} value is much closer to case 2) and TaB_2 is the most like case 2. All of these diborides have ^{11}B V_{zz} values ranging from <0.065 to 1.722×10^{21} V/m^2, i.e. values that indicate that the metal atoms donate electrons to the boron atoms. These data also underscore the importance of the partially covalent M-B bonding, seeing that the experimental ^{11}B V_{zz} values fall between the extreme models of predominance of covalent B-B bonding or predominance of metallic M-M bonding.

4.2.2. Comparison of ^{11}B quadrupole coupling constant with lattice parameters and cell volume

Based solely on TiB_2 and ZrB_2 ^{11}B NMR data, Silver [23,25] hypothesised that (within Group IV) the structure with the largest lattice spacing (i.e. M-B distance or M-M distance, in Group IV this is ZrB_2) should have the least lattice contribution to V_{zz}, i.e. larger lattice spacing, smaller ^{11}B EFG. With the benefit of the entire data set for this series, this hypothesis is not supported by the ^{11}B NMR data in Fig. 13 (b) when compared with the M-B data in Table 2 and Supplementary Fig. S19. Carter and Swartz [30] tested their ^{11}B C_q data for correlations with lattice parameters and cell volume, concluding that, "*The quadrupole coupling constant of ^{11}B across both 3d and 4d series does not correlate with the c/a ratio or unit cell volume. This may indicate deviation of the boron atoms from a planar configuration.*" Note that Carter and Swartz included MoB_2 in their 4d Period—hence the comment on non-planar boron configuration. From Table 1, the entire data set, including 3s, 3d, 4d, and 5d diborides, all with planar boron configuration in the AlB_2-type structure group 191, indicates no correlation of ^{11}B quadrupole coupling constant with lattice parameters or cell volume. If the lattice contribution to the EFG were dominant over the valence electron contribution, then the ^{11}B C_q would be expected to be sensitive to the lattice constants. Calculations of the EFG at the boron site also indicate that the ^{11}B V_{zz} is dominated by the valence boron p electrons, except in the case of TaB_2 where the lattice and electron contributions are similar and the ^{11}B V_{zz} is very small [103].

By comparison, rare earth metal and alkaline earth metal hexaborides show systematic change in ^{11}B V_{zz} values as a function of lattice parameter due to a consistent 30% and 40% contribution from the lattice, respectively (see Bastow et al. [119]) [39,120]. In the case of the diborides, the lattice contribution is not consistent—it is smallest for MgB_2 at 3%, increasing to 54% for TaB_2 as calculated by Medvedeva et al. [103]. The ^{11}B V_{zz} values in the diborides do not follow the lattice parameters, cell volume, M-B distance, or metal atomic number, but they do follow the metal site V_{zz} values as shown in Fig. 13 (c and d), and

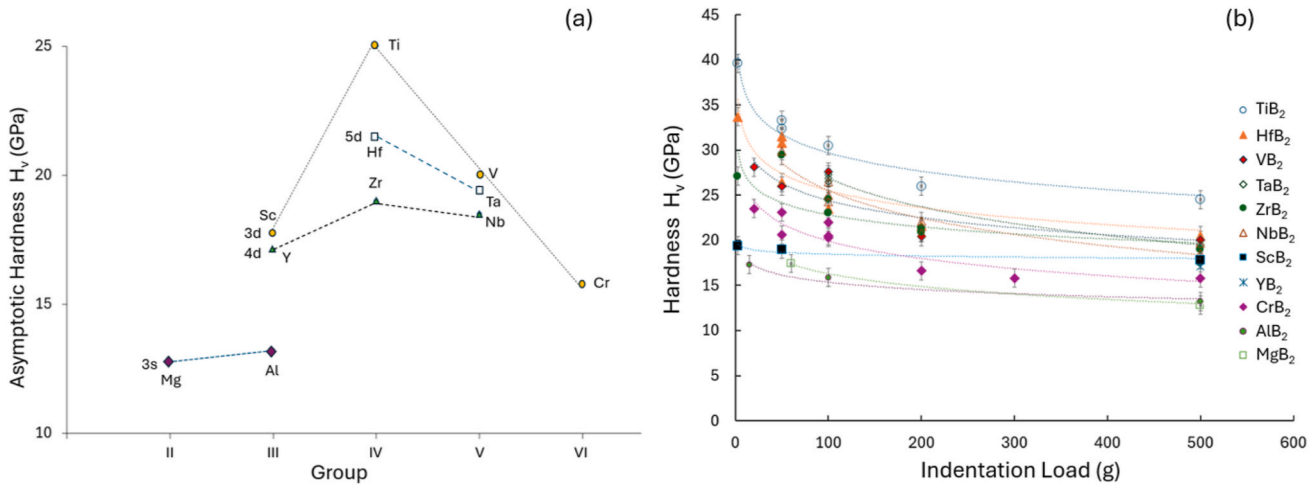

Fig. 15. (a) Asymptotic bulk hardness data for AlB_2 structure-type metal diborides from Table 2 and (b) hardness as a function of indentation load (2.5 to 500 g) modelled with logarithmic fits (data from Supplemental Table S15.2).

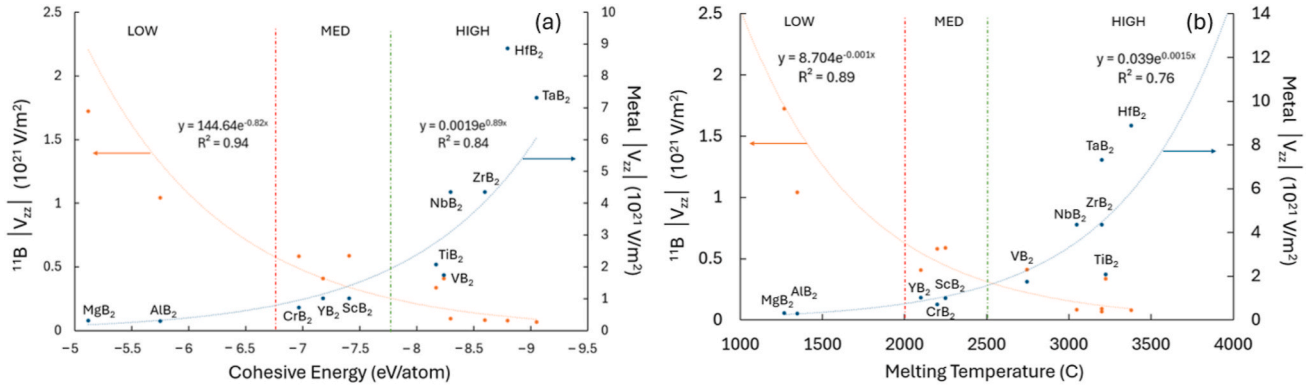

Fig. 16. Metal site V_{zz} and ^{11}B V_{zz} experimental data as exponential functions of **(a)** cohesive energy and **(b)** melting point temperature, for these isomorphous diborides showing grouping into low, medium, and high bands.

the relationship is a power law. There are two regions at the edges of the relationship where the ^{11}B and metal V_{zz} trends do not completely mirror each other—the main group metals and the 5d metals. The lattice contribution to the ^{11}B V_{zz} is smallest in the main group metal diborides [103], and the ^{11}B V_{zz} values are the smallest in the 5d Period metal diborides. The range of the ^{11}B V_{zz} values in this metal diboride series indicates that the metal (M) is donating valence electrons to the boron (B) atoms, populating hybrid bonding and antibonding orbitals.

4.2.3. Cohesive-related properties in these metal diborides

As mentioned in Sec. 1.1, the role of the metal atom, as electron donor or acceptor in establishing bonding character, was the study of much early work in the diborides [10,47,49,110,121]. The remarkable change in melting temperature, T_m, from the pure parent metals to the AlB_2-structure type diborides prompted such studies [77]. The melting temperatures of the pure metals are raised by incorporation of the boron layer—in the case of the Group IV hcp parent metals Ti, Zr, Hf, by more than 1100 °C with the other hcp parent metals Mg, Sc, Y raised by 500 to 700 °C on becoming diborides. The body centered cubic (bcc) parent metals V, Nb, Cr, and Ta, already have relatively high melting point temperatures and, even so, they are raised by 300 to 800 °C by incorporation of the boron layer to form the diboride. Al is the only face centered cubic (fcc) parent metal, and its T_m is raised by 700 °C.

The transition metal diborides in this series are ultrahigh temperature refractory metals with melting point temperatures $T_m \geq 2000$ °C and asymptotic bulk hardness values $H_v \geq 15$ GPa. The main group metal diborides, although lower in T_m and H_v values, have cohesive properties that are correlated with the transition metal diborides. Comparison of the calculated cohesive energies of the metal diborides with those of the parent metals shows an increase of the energy needed to break bonds due to the incorporation of the boron layer. The cohesive energy is calculated as the energy per atom in its ground state at 0 K for the hcp crystal structure for the parent metals and the metal diborides [84–86,122]. Fig. 14 (a and b) shows the experimental melting point temperatures and calculated cohesive energies of these diborides and the pure parent metals.

Bond strength should be reflected in cohesive properties such as melting point and hardness, and as discussed in Sec. 1.1, there is a correlation among melting point, asymptotic hardness, and calculated cohesive energy values given in Table 2 for this set of isomorphous diborides. In the present work, experimental physical properties of these compounds have been compiled from the literature for high purity, high density diboride samples in order to examine the correlation of NMR parameters with cohesive properties.

Hardness values within this isomorphous series of metal diborides should reflect the strength of the metal-boron (M-B) bonds, where the greater the bond strength the greater the ability to resist shear. The hardness measurement method can influence the physical property, because hardness is a function of the indentation load for these diboride compounds. For that reason, it is important to compare asymptotic bulk hardness values, i.e. values for indentation loads >300 g to 500 g in the region where there is little variation of hardness with load [3]. For the present work, literature values of hardness for high purity, high density materials from published data sets have been compiled using a range of

indenter loads (see Supplemental Tables S15.1 and S15.2). The hardness values in Fig. 15 (a) are asymptotic values for an indenter load of 500 g (4.9 N), see Fig. 15 (b). Several research teams have studied subsets of this series of metal diborides [3,123–129] and a clear ranking emerges, with the group IV and V transition metal diborides TiB_2, HfB_2, VB_2, TaB_2, ZrB_2, and NbB_2 at the higher hardness end of the scale, the Group III and VI transition metal diborides ScB_2, YB_2, and CrB_2 in the middle, and the main group metal diborides MgB_2 and AlB_2 at the lower hardness end of the scale. Fig. 14 (a) shows that the melting point temperatures cluster similarly into the three bands (high, medium, low) for the diborides, as do the V_{zz} values of Fig. 13 (a and b) with one exception that VB_2 just falls into the medium band for the ^{11}B V_{zz} data. The inflection at Group IV in these cohesive properties (Fig. 14 (a and b) and Fig. 15 (a)) is indicative of the transition from filling of bonding states to filling of antibonding states. This clustering of compounds, into the high, medium, and low end of the cohesive property scale is also apparent in the comparison of experimental V_{zz} values with calculated cohesive energy values and measured melting point temperatures as shown in Fig. 16 (a and b), supporting a relationship between bond strength and the EFG values at the boron and metal sites as measured by NMR.

It has been shown that the boron and metal site V_{zz} values can be correlated with cohesive properties, separating into high, medium, and low groupings. Correlating the metal diboride NMR C_q and V_{zz} parameters with cohesive properties may be helpful to the future development of material property descriptors from these NMR data, for example descriptors that can predict structural materials that can overcome structure-property trade-offs such as hardness and fracture toughness, perhaps as a function of composition.

4.2.4. Comparison of B site and metal site EFG data with bonding calculations

The 'best' data sets for B site and M site V_{zz} values tend to mirror each other as seen by comparing Fig. 13 (a and b) and have a power law relationship as shown in Fig. 13 (c and d). The values of ^{11}B V_{zz}, when compared to values from the two extreme models calculated for B-B bonding dominance or M-M bonding dominance, indicate that M-B bonding plays an important role in these EFGs [25]. Bonding character in these diborides is a topic of great interest [10,11,13,37,51,130–133]. Computational work has focussed on the bonding character of the metal layers (metallic), the boron layers (covalent), and the metal-boron interlayer bonding (ionic-covalent). Methods of calculating bonding character aim to account for the charge distribution in these compounds, band filling effects, and hybridization [9,10,12,13,37,103]. Wang et al. [37] calculated the band structures for nine of these transition metal diborides suggesting that the hybridization of the transition metal d states with the boron p states increases systematically with Period in the Group, however, the extent of hybridization was not quantified. To move from qualitative to quantitative bonding parameters, it has been suggested that the extent of hybridization is determined by the electron donor ability of the metal atoms, and that the amount of electron transfer correlates with the strength of the M-B bond in these metal diborides [49,134]. The donor ability of the metal has been assessed by calculation of the effective charge on the atoms by several research groups giving variable results [10,13,49,84] most likely attributable to the approximations used in the chemical calculations. Wagner et al. [13] have calculated the effective charges using the Bader quantum theory of atoms in molecules (QTAIM) method for all of the diborides in this isomorphous series showing that the effective charge on the atoms varies monotonically (see Supplementary Figures S20.1 and S20.2). The metal and boron charges mirror each other. The relationship between the effective metal and boron charges is linear. The delocalization index, calculated using the Bader QTAIM method, also known as an effective covalent bond order, can be used to quantify electron sharing for the B-B, M-B, and M-M bonding interactions in this series [13]. The M-B covalent electron sharing parameter shows systematic and monotonic increases in covalency with Period and Group as shown in Supplementary Figures S20.3 and S20.4 [13]. The M-B, B-B, and M-M bond order parameters calculated by Wagner et al. [13] fail to capture the EFG trends for the 3d and 4d Periods that are relevant to the correlation of V_{zz} with cohesive properties in these compounds (see Fig. 16 (a and b) and Supplementary Figures S20.3 and S20.4). It can be noted that earlier methods of M-B bond order calculation [10,53] for subsets of this isomorphous series give results that differ from that of Wagner et al. [13], in the trends of the 3d and 4d Periods (Supplementary Figures S20.3 and S20.4). It is hoped that the NMR data for this entire set of isomorphous metal diborides will assist with modelling electron interactions in these compounds.

4.3. Comparison of experimental and calculated interactions

4.3.1. Knight shift

Measurement of the Knight shifts can help benchmark *ab initio* quantum chemical methods for calculating Knight shifts. DFT calculation of the Knight shift (K_{iso}) requires a very accurate description of the electronic structure to predict magnetic shielding, and the relativistic nature of electrons and the reference scale are involved. The accuracy of the magnetic shielding tensor calculations depends on the accuracy of the computed ground state and excited state electron densities using, for example, GIPAW, PAW, etc. The amount of exchange incorporated in the DFT calculations also affects K_{iso}, and comparison of experiment and theory can be used to quantify that exchange. The metal and boron Knight shifts for MgB_2 and AlB_2 have been calculated *ab initio* and with numerical methods, showing limited agreement with the experimental data [38,41]. The discussion in Sec. 4.1 for the full set of experimental K_{iso} results has highlighted the role of conduction electrons in the covalent bonding and the importance of d states. Laskowski and Blaha [35] have successfully calculated K_{iso} values for some pure transition metals, with both orbital and spin contributions needed to find agreement with the experiment. Calculation of Knight shifts in transition metal diborides is still tentative and, although outside the scope of this work, it is hoped that access to the experimental data set for this isomorphous series will stimulate such calculations to settle some debate, as well as create new hypotheses and topics for further study.

4.3.2. Quadrupolar coupling constant and EFG

Typically, the calculated C_q and V_{zz} values either systematically overestimate or underestimate the experimental ones due to limitations of the theoretical approach used [65]. The calculations in Table 1 and Fig. 13 (d) (data in Supplementary Table S7) were completed prior to knowledge of the 'best' experimental data set for ^{11}B and metal site V_{zz} values. Although the EFG values calculated for each atomic site in the AlB_2-type crystalline structure reflect the unique local electronic and nuclear environment surrounding that atom, Fig. 13 (d) shows that the calculated boron and metal site EFG values are related. The EFG value at the atom is determined by the distribution of electron density and the positions of the other atoms in the lattice. Significant shift in charge from the metal site to the boron site modifies the local electron density at the nucleus. The effective charge at the metal and the boron, as calculated by Wagner et al. [13] and others [10,49,84], can be described by equation $B = -0.5M$, where B is the effective charge on the boron, and M is the effective charge on the metal which varies from 0.89 (for Cr) to 2.15 (for Al) (see Supplementary Fig. S20). As discussed in Sec. 4.2.4, the calculated effective charge and covalency parameters [13] fail to capture the relationships between the EFG values at the metal and boron sites and the relationships between the EFG values and the cohesive properties in these metal diborides. The power law relationship given in Fig. 13 (c and d) for these compounds means that accurate measurement or calculation of the EFG value at the boron site can then give an accurate prediction for the metal site V_{zz} in these diborides. Fig. 13 (d) shows calculated values that are outliers from the 'best' experimental values. In the case of TaB_2 it is the calculated ^{11}B V_{zz} values that are too low in the work of Schwarz [39] and Haas [69]. For YB_2, there are no

published ^{11}B spectra in the literature, and the ^{89}Y V_{zz} cannot be measured because ^{89}Y is spin ½ and has no quadrupole moment. It is likely that the calculated values for ^{89}Y V_{zz} from the work of Choudhary [104] and Haas [69] are low, therefore, future research is suggested. For AlB_2, the DFT calculations reviewed here are unable to predict the ^{27}Al V_{zz} value, as discussed in Sec. 3.5. Access to the entire experimental data set allows systematic testing of DFT approximations including exchange correlation effects, empirical parameters, and relaxed lattice parameters—such testing is suggested as potentially fruitful future work.

The valence and lattice contributions to the ^{11}B V_{zz} values have been computed by Medvedeva [103] for seven of these diborides, indicating a dominant contribution from the valence boron p electrons in all but TaB_2 where the lattice and valence contributions are similar. The pure metal V_{zz} values have been calculated for five of the hcp parent metals in this series using DFT [109,135] indicating dominance of the valence contribution (the p orbital contribution) over the lattice contribution. The valence and lattice contributions to the ^{11}B V_{zz} and metal site V_{zz} values for the entire isomorphous series have not been calculated and such work is suggested as fruitful future work.

5. Conclusions

Multinuclear solid-state NMR and zero field NQR results for AlB_2-structure type metal diborides have been presented and correlated with physical and electronic properties. The NMR and NQR measurements, through their relationship to the metal-boron hybridization, M-B bond covalency, and d-band characteristics, have provided experimental constraints on measured and calculated physical properties for this isomorphous series. The correlation of the metal diboride NMR C_q and V_{zz} parameters with the cohesive properties of melting point and asymptotic bulk hardness relies on the quadrupole interaction being determined by the spatial distribution of ground state electronic charge at the nucleus that plays a dominant role in bond strength. The correlation of the metal site K_{iso} with d-band center and catalytic activity relies upon the Knight shift being determined by the electrons near the Fermi surface influencing core polarization and the catalytic activity of the material. These correlations are promising, and development of semi-empirical and theoretical relationships between the NMR interactions and the physical and electronic properties of these metal diborides is left for future work.

The availability of high-quality experimental NMR data for this entire set of eleven isomorphous metal diborides, for both the metal and boron sites, has allowed rigorous testing of bonding hypotheses. These metal diborides are the subject of much current study for use as catalysts [15,19,56] and hypersonic materials [136], where manipulation of the electronic and structural properties through defect engineering, alloying, and strain are useful methods of property optimisation. In that regard, this set of NMR measurements should help guide the refinement of DFT approaches and parametric descriptors for predictive calculations, in addition to guiding experimental approaches to materials design for related compounds.

This study has reported NMR quadrupolar interaction parameters for the first time for several metal diborides and reanalysed the best data in the literature to produce the most comprehensive set of NMR data yet reported from these diborides. The data represent the first report of $^{27}AlB_2$ satellite singularities to define $C_q = 1.03$ MHz and $V_{zz} = 0.291 \times 10^{21}$ V/m^2. First-order C_Q values of 0.480 to 0.533 MHz had been previously reported for $^{27}AlB_2$ [29,38] without publication of the corresponding $^{27}AlB_2$ spectra. Measurement of the $^{27}AlB_2$ first-order C_q (and V_{zz}) from our NMR experiment challenges the choice of DFT parameters used to calculate V_{zz}, as the reported calculations to date, including ours in the present work, are 3 to 7 times lower than the experimental value. This study now allows all experimentally measured quadrupolar coupling constants at both metal and boron sites to be compared with first principle calculations for this isomorphous set of metal diborides. The experimental versus theoretical comparison in the present work shows a high degree of correlation. The exception, that gives rise to future work, is the prediction of the EFG at the metal site in $^{27}AlB_2$. In addition, of the DFT approaches compared in this work, none is consistently accurate across the entire data set, suggesting future work on the choice of functionals, approximations, and energy cut-offs.

The present work includes the first report of $^{181}TaB_2$ $C_q = 560$ MHz and $V_{zz} = 7.306 \times 10^{21}$ V/m^2 from NMR measurements and $^{177}HfB_2$ $C_q = 721$ MHz and $V_{zz} = 8.875 \times 10^{21}$ V/m^2 from NQR measurements, which can be considered preliminary results. The time-consuming frequency stepping method was used to identify singularities in $^{181}TaB_2$ and only a single weak echo was found for $^{177}HfB_2$. Further work is suggested to measure additional singularities in order to reduce the error in the metal site C_q and V_{zz} values for HfB_2 and TaB_2 reported here. Future work is also suggested to measure the metal Knight shifts in ^{177}Hf pure metal, $^{177}HfB_2$, and $^{181}TaB_2$ to refine the best estimates for these parameters from the correlation established in Sec. 4.1.

New data, analyses, and discussion of the ^{11}B central line splitting in these diborides have been contributed, suggesting that the splitting is likely to be a Pake doublet reflecting the B-B distance, as first put forward by Torgeson et al. [70]. We note that other reports have attributed the splitting of the ^{11}B central line in AlB_2-type metal diborides to boron in the coil [30,40] or to paramagnetic defects [74]. Although we are not able to present a systematic measurement series of ^{11}B doublets for this isomorphous set of diborides, the present work highlights numerous reports of splitting detected in the ^{11}B central peak of AlB_2-structure type diborides noting that the peak-to-peak distance can be correlated with the B-B distance (Sec. 3.3)—a trend supportive of the Pake doublet attribution suggested here. More sophisticated NMR experiments, specifically designed to study internuclear distances [137], are suggested as fruitful future work.

In addition to highlighting areas for further NMR research, our full comparison of theory and experiment for high quality specimens of these isomorphous metal diborides points to areas where further characterization is required, both theoretical and experimental. Hardness measurements as a function of indentation load to at least 500 g (4.9 N) in high quality samples of AlB_2 and YB_2 would fill a gap in the literature. In separating this set of compounds into high, medium, and low cohesive-type properties based on the ^{11}B and metal site V_{zz} values, the compound VB_2 sometime falls into the medium band even though its hardness and melting temperature should place it in the high band (see Supplementary Fig. S21). Further calculations of bond energies or bond strengths to shed light on the non-monotonic behavior of V_{zz} values and bonding parameters for the 3d Period (Fig. 13) could help further elucidate the role of the EFG in probing the bond strength for these compounds. Bester [115] has calculated bonding states in MgB_2 and AlB_2, noting that the d orbitals of the metal atoms make a non-negligible contribution to M-B bonding. Calculation of d-center values for MgB_2 and AlB_2 could help refine the relationship between metal site K_{iso} and d-band center put forward in Fig. 12 (c).

NMR and NQR have been used to characterise these critical metal diborides generating new knowledge of quadrupolar interactions potentially useful in technologies for value-added critical metal production or recycling from end-of-life products. As society transitions to efficient and responsible valorisation of materials (refining, reuse, recovery, recycle), an ability to rapidly scan and identify materials and their bonding, including important critical metal materials, is needed. For the set of critical metals examined here, the present work has illustrated that magnetic resonance could provide such a fingerprinting method [7,8].

Author contributions

TJB devised the experimental plan, contributed the overall supervision of this work, and performed NMR and NQR measurements, data analysis, and co-wrote the manuscript. AJH assisted in data collection and analysis and co-wrote the manuscript. STH and RWS performed DFT

calculations and edited the manuscript. AS performed XRD measurements and analysis and edited the manuscript. AT, KMN, RJM, and MES assisted in completing the data analysis and edited the manuscript.

Data statement

The authors confirm that the data supporting the findings of this study are available within the article and its supplementary materials.

Declaration of competing interest

The authors declare that they have no known competing financial interests or personal relationships that could have appeared to influence the work reported in this paper.

Acknowledgements

We gratefully acknowledge CSIRO: Lyndsey Benson is thanked for her support of the work as the leader of the Functional Powders team at CSIRO. MES thanks both the University of Southampton and EPSRC for supporting his research. STH and RWS acknowledge support from The Florida State University and the National High Magnetic Field Laboratory (NHMFL), which is funded by the National Science Foundation Cooperative Agreement (DMR-2128556) and the State of Florida. Sadly Robert W. Schurko died while the manuscript was under review. The authors are grateful to Timothy J. Bastow, sadly now deceased, for sharing his passion for magnetic resonance with them. Tim died in the final stages of data collection and manuscript preparation. It is very fitting that this manuscript is submitted to a special issue marking the many contributions of Jeff Reimer. Jeff's sustained and innovative contributions to solid-state NMR are greatly admired by the authors, including CSIRO colleagues past and present who remember Jeff's generous support for Tim Bastow's and Geoff West's development of a wide-bore multinuclear solid-state NMR facility in Australia in the 1980s.

Appendix A. Supplementary data

Supplementary data to this article can be found online at https://doi.org/10.1016/j.ssnmr.2026.102091.

Data availability

The authors confirm that the data supporting the findings of this study are available within the article and its supplementary materials.

References

[1] E.A. Cernak, The oxidation of Cr, Hf, Mo, Nb, Ta, Ti, N, V, Zr and some of their alloys; properties of some borides, carbides, nitrides, and oxides of the same metals. A bibliography 1952-1959, Pratt and Whitney Aircraft Division Library, Connecticut Operations-CANEL (1959) 1–98. CNLM-1802-5: Middletown, CN, USA, https://www.osti.gov/servlets/purl/4188894.

[2] C. May, Stability of Ceramics in Hydrogen Between 4000 and 4500 F. NASA Memo 3-5-59E, 1959. Document ID 19980228142, https://ntrs.nasa.gov/citations/19980228142.

[3] L. Kaufman, E. Clougherty, Investigation of boride compounds for very high temperature applications, Technical Report RTD-TDR-63-4096, Part 1, AFML, WPAFB, OH, https://apps.dtic.mil/sti/tr/pdf/AD0461864.pdf, Dec. 1963.

[4] A.L. Ivanovskii, Mechanical and electronic properties of diborides of transition 3d–5d metals from first principles: toward search of novel ultra-incompressible and superhard materials, Prog. Mater. Sci. 57 (2012) 184.

[5] M. Magnuson, L. Hultman, H. Högberg, Review of transition-metal diboride thin films, Vacuum 196 (2022) 110567.

[6] J.T. Doane, G.M. John, A. Kolakji, A.A. Rosenberg, Y. Zhang, A.A. Chen, M. T. Yeung, Violations of coordination: exploring metastable diborides via energetic transition metals, J. Am. Chem. Soc. 147 (2025) 16578–16584.

[7] J.A. Lehmann-Horn, D.G. Miljak, L.A. O'Dell, R. Yong, T.J. Bastow, Rapid detection of arsenic minerals using portable broadband NQR, Geophys. Res. Lett. 41 (19) (2014) 6765.

[8] T.J. Bastow, J. Lehmann-Horn, D.G. Miljak, ^{121,123}Sb and ^{75}As NMR and NQR investigation of the tetrahedrite ($Cu_{12}Sb_4S_{13}$) - tennantite ($Cu_{12}As_4S_{13}$) system and other metal arsenides, Solid State Nucl. Magn. Reson. 71 (2015) 55, https://doi.org/10.1016/j.ssnmr.2015.09.010.

[9] A.F. Guillermet, G. Grimvall, Bonding properties and vibrational entropy of transition metal MeB_2 (AB_2) diborides, J. Less Common. Met. 169 (1991) 257–281.

[10] F.L. Carter, Valence bonding in some refractory transition metal compounds with high coordination, in: R.S. Roth, S.J. Schneider (Eds.), NBS Special Publication Issue 364 Solid State Chemistry, 1971, p. 515. NBS Washington, D.C.

[11] J.K. Burdett, E. Canadell, G.J. Miller, Electronic structure of transition-metal borides with the AlB_2 structure, J. Am. Chem. Soc. 108 (1986) 6561.

[12] P. Vajeeston, P. Ravindran, C. Ravi, R. Asokamani, Electronic structure, bonding, and ground-state properties of AlB_2-type transition-metal diborides, Phys. Rev. B 63 (2001) 045115, https://doi.org/10.1103/PhysRevB.63.045115.

[13] F.R. Wagner, A.I. Baranov, Y. Grin, M. Kohout, A position-space view on chemical bonding in metal diborides with AlB_2 type of crystal structure, Z. Anorg. Allg. Chem. 639 (11) (2013) 2025–2035.

[14] D.M. Hoat, Electronic structure, chemical bonding, optical, elastic and dynamical properties of MeB_2 compounds: effect of transition metal me = Sc, Ti, and Zr, Comput. Condens. Matter 21 (2019) e00406.

[15] Q. Li, X. Zou, X. Ai, H. Chen, L. Sun, X. Zou, Revealing activity trends of metal diborides toward pH-universal hydrogen evolution electrocatalysts with Pt-like activity, Adv. Energy Mater. 9 (5) (2019) 1803369, https://doi.org/10.1002/aenm.201803369.

[16] W.B. Pearson, The stability of metallic phases and structures: phases with the AlB_2 and related structures, Proc. R. Soc. Lond., Ser. A Math. Phys. Sci. 365 (1723) (1979) 523–535.

[17] V. Moraes, R. Helmut, C. Fuger, P. Polcik, H. Bolvardi, D. Holec, P.H. Mayrhofer, Ab initio inspired design of ternary boride thin films, Sci. Rep. 8 (2018) 9288, https://doi.org/10.1038/s41598-018-27426-w.

[18] S. Chakrabarty, A. Thakur, A. Rasyotra, B. Gaykwad, K. Jasuja, Quasi-two-dimensional nanostructures from AlB_2-type metal borides: physicochemical insights and emerging trends, J. Phys. Chem. C 127 (2023) 852.

[19] E. Sadeghi, S. Chamani, N.S. Peighambardoust, U. Aydemir, Unveiling the potential of metal diborides for electrocatalytic water splitting: a comprehensive review, Energy Environ. Mater. 8 (2025) e12873, https://doi.org/10.1002/eem2.12873.

[20] M.J. Gasch, D.T. Ellerby, S.M. Johnson, Ultra high temperature ceramics. Ch 9, in: N.P. Bansal (Ed.), Handbook of Ceramic Composites, Kluwer Academic Publ, Boston, 2005, pp. 197–224. https://link.springer.com/book/10.1007/b104068.

[21] X.-Q. Chen, C.L. Fu, M. Krčmar, G.S. Painter, Electronic and structural origin of ultra-incompressibility of 5d transition-metal diborides MB_2 (M = W, Re, os), Phys. Rev. Lett. 100 (2008) 196403, https://doi.org/10.1103/PhysRevLett.100.196403.

[22] A.H. Silver, Nuclear Quadrupole Effects in Boron Compounds, Rensselaer Polytechnic Institute, 1958. PhD Thesis.

[23] A.H. Silver, P.J. Bray, NMR study of bonding in some solid boron compounds, J. Chem. Phys. 32 (1960) 288–292.

[24] O.T. Malyuchkov, V.A. Povitskii, Nuclear magnetic resonance study of transition metal borides and pure boron, Poroshkovaya Metall. 4 (10) (1962) 26–34.

[25] A.H. Silver, T. Kushida, Nuclear magnetic resonance in transition-metal diborides, J. Chem. Phys. 38 (1963) 865–872.

[26] R.B. Creel, Nuclear Magnetic Resonance in Transition Metal Borides, PhD Thesis, Iowa State University, 1969, https://www.osti.gov/servlets/purl/4147843.

[27] R.G. Barnes, R.B. Creel, Chromium-like antiferromagnetic behavior of CrB_2, Phys. Lett. A. 29 (1969) 203.

[28] R.G. Barnes, R.B. Creel, D.R. Torgeson, Nuclear magnetic resonance in the diborides of scandium and yttrium, J. Chem. Phys. 53 (1970) 3762–3763.

[29] J.P. Kopp, R.G. Barnes, Nuclear magnetic resonance of ^{11}B and ^{27}Al in alumAnum diboride, J. Chem. Phys. 54 (1971) 1840–1841.

[30] G.C. Carter, J.C. Swartz, Nuclear magnetic resonance knight shifts and quadrupole effects in transition metal diborides, J. Phys. Chem. Solids. 32 (1971) 2415.

[31] K.J.D. MacKenzie, M.E. Smith, Multinuclear solid state NMR of inorganic materials, in: Pergamon Materials Series, vol. 6, Pergamon, An Imprint of Elsevier Science, Amsterdam, 2002.

[32] M.E. Smith, E.R.H. van Eck, Recent advances in experimental solid state NMR methodology for half integer spin quadrupolar nuclei, Prog. Nucl. Magn. Reason. Spectrosc. 34 (1999) 159–201.

[33] P. Pyykkö, Year-2017 nuclear quadrupole moments, Mol. Phys. 116 (2018) 1328.

[34] P. Blaha, K. Schwarz, G.K.H. Madsen, D. Kvasnicka, J. Luitz, WIEN2k, an Augmented Plane Wave plus Local Orbitals Program for Calculating Crystal Properties, Vienna University of Technology, Vienna, Austria, 2001.

[35] R. Laskowski, P. Blaha, NMR shielding in metals using the augmented plane wave method, J. Phys. Chem. C 119 (2015) 19390.

[36] B.D. Hanson, M. Mahnig, L.E. Toth, Low temperature heat capacities of transition metal borides, Z. Naturforsch. 26 (1971) 739.

[37] X.-B. Wang, D.-C. Tian, L.-L. Wang, The electronic structure and chemical stability of the AlB_2-type transition metal diborides, J. Phys. Condens. Matter 6 (1994) 10185.

[38] S.H. Baek, B.J. Suh, E. Pavarini, F. Borsa, R.G. Barnes, S.L. Bud'ko, P.C. Canfield, NMR spectroscopy of the normal and superconducting states of MgB_2 and comparison to AlB_2, Phys. Rev. B 66 (2002) 104510.

[39] K. Schwarz, H. Ripplinger, P. Blaha, Electric field gradient calculations of various borides, Z. Naturforsch. 51a (1996) 527–533.

[40] T.J. Bastow, ^{25}Mg NMR determination of knight shift, spin-lattice relaxation and electric field gradient in MgB_2, Solid State Commun. 124 (2002) 269.
[41] E. Pavarini, S.H. Baek, B.J. Suh, F. Borsa, S.L. Bud'ko, P.C. Canfield, NMR relaxation rates and knight shifts in MgB_2 and AlB_2: theory versus experiments, Supercond. Sci. Technol. 16 (2003) 147–151.
[42] T.J. Bastow, M.A. Gibson, C.T. Forwood, ^{47,49}Ti NMR: hyperfine interactions in oxides and metals, Solid State NMR 12 (1998) 201.
[43] T.J. Bastow, A.J. Hill, K.M. Nairn, M.E. Smith, ^{53}Cr solid-state nuclear magnetic resonance: new observations and comprehensive correlations as a probe of valence and magnetic states, Phys. Rev. Mater. 7 (2023) 114410.
[44] C.S. Lue, W.J. Lai, NMR study of B-2p Fermi-level density of states in the transition metal diborides, phys. stat. sol. (b) 242 (2005) 1108–1112, https://doi.org/10.1002/pssb.200402136.
[45] S. Paluch, O.J. Zogał, P. Peshev, Low electron density of states at the boron site of TMB_2 (TM = Ti, Zr, Hf, and Nb): a ^{11}B NMR study, J. Alloys Compd. 383 (2004) 176–179.
[46] N. Barbero, T. Shiroka, B. Delley, T. Grant, A.J.S. Machado, Z. Fisk, H.-R. Ott, J. Mesot, Doping-induced superconductivity of ZrB_2 and HfB_2, Phys. Rev. B 95 (2017) 094505.
[47] L.H. Bennett, A.J. McAlister, R.E. Watson, Interstitial compounds, Phys. Today 34 (1977: September).
[48] S.H. Lui, L. Kopp, W.B. England, H.W. Myron, Energy bands, electronic properties, and magnetic ordering of CrB_2, Phys. Rev. B 11 (9) (1975) 3463.
[49] G.V. Samsonov, B.A. Kovenskaya, in: Matkovich VI (Ed.), The Electronic Structure of Boron Compounds. the Nature of the Chemical Bonds in Borides. Chapters I and II in Boron and Refractory Borides, Springer Verlag, New York, 1977, pp. 5–30.
[50] J. Castaing, P. Costa, M. Hertier, P. Lederer, Spin fluctuation effects in nearly antiferromagnetic vanadium and chromium diborides, J. Phys. Chem. Solids. 33 (1972) 533.
[51] K.E. Spear, Chemical bonding in AlB_2-type borides, J. Less-Common Metals 47 (1976) 195–201.
[52] G.V. Samsonov, Y.M. Goryachev, B.A. Kovenskaya, Electronic structure and chemical bonding in transition element borides, J. Less-Common Metals 47 (1976) 147.
[53] A.M. Mulokozi, Electron transfer and bonding in the transition metal diborides the heats of formation of the metal diborides derived from a theoretical bonding model, J. Less-Common Met. 64 (1979) 145–153.
[54] L. Topor, O.J. Kleppa, Enthalpies of formation of first-row transition-metal diborides by a new calorimetric method, J. Chem. Thermodynamics. 17 (1985) 1003–1016.
[55] X.L. Chen, Q.Y. Tu, M. He, L. Dai, L. Wu, The bond ionicity of MB_2 (M = Mg, Ti, V, Cr, Mn, Zr, Hf, Ta, Al and Y), J. Phys. Condens. Matter 13 (2001) L723–L727.
[56] Z. Li, B. Zhao, L. Wang, Q. Tao, P. Zhu, Mechanical properties and multifunctionality of AlB_2-type transition metal diborides, J. Phys. Condens. Matter 35 (2023) 074002.
[57] R.B. Creel, R.G. Barnes, Nuclear magnetic resonance study of transition metal monoborides. I. ^{11}B nuclear electric quadrupole interaction parameters, J. Chem. Phys. 56 (1972) 1549.
[58] T.J. Bastow, M.E. Smith, S.N. Stuart, Observation of ^{91}Zr NMR in zirconium-based metals and oxides, Chem. Phys. Lett. 191 (1992) 125.
[59] T.J. Bastow, Materials Characterisation by Nuclear Quadrupole Interaction, Z Naturforsch, 1994, p. 320, 49a.
[60] T.J. Bastow, C.T. Forwood, M.A. Gibson, M.E. Smith, Local site symmetry and electronic structure of trialuminide and related intermetallic alloys probed by solid-state NMR, Phys. Rev. B 58 (1998) 2988–2997.
[61] R.W. Schurko, Ultra-wideline solid-state NMR spectroscopy, Accounts of Chemical Research 46 (9) (2013) 1911.
[62] P.T. Callaghan, Principles of Magnetic Resonance Microscopy, Clarendon Press, Oxford, 1991, p. 73.
[63] M.C. Morris, H.F. McMurdie, E.H. Evans, B. Paretzkin, Standard x-ray Diffraction Powder Patterns: Section 17 - Data for 54 Substances, National Institute of Standards and Technology, Gaithersburg, MD, 1980, p. 66, https://doi.org/10.6028/NBS.MONO.25-17. Monograph no 25/17.
[64] T. Su, C. Lue, Y. Kuo, NMR and Seebeck coefficient studies of the electronic band structure in $Nb_{1-x}B_2$, J. Appl. Phys. 104 (2008) 093705.
[65] S.T. Holmes, R.W. Schurko, Refining crystal structures with quadrupolar NMR and dispersion-corrected density functional theory, J. Phys. Chem. C 122 (3) (2018) 1809–1820, https://doi.org/10.1021/acs.jpcc.7b12314.
[66] R.G. Barnes, D.R. Torgeson, P.J. Bray, On NMR powder spectrum simulation for nuclei with I > ½, phys. stat. sol. (b) (1988) K175, 147.
[67] D. Massiot, F. Fayon, M. Capron, I. King, S. Le Calvé, B. Alonso, J.-O. Durand, B. Bujoli, Z. Gan, G. Hoatson, Modelling one- and two-dimensional solid-state NMR spectra, Magn. Reson. Chem. 40 (2002) 70–76.
[68] T.F. Kemp, M.E. Smith, QuadFit—A new cross-platform computer program for simulation of NMR line shapes from solids with distributions of interaction parameters, Solid State Nucl. Magn. Reson. 35 (4) (2009) 243–252.
[69] H. Haas, Electric field gradients in metal diborides, Hyperfine Interact. 136/137 (2001) 731–735.
[70] D.R. Torgeson, R.G. Barnes, R.B. Creel, NMR study of $ThAl_2$: ^{27}Al, dipolaa doublet, quadrupole, and anisotropic shift interactions, J. Chem. Phys. 56 (1972) 4178–4183.
[71] G.E. Pake, Nuclear resonance absorption in hydrated crystals: fine structure of the proton line, J. Chem. Phys. 16 (4) (1948) 327–336.
[72] C. Michioka, Y. Itoh, K. Yoshimura, Y. Watabe, Y. Kousaka, H. Ichikawa, J. Akimitsu, NMR studies of single crystal chromium diboride, J. Magn. Magn Mater. 310 (2007) e620–e622.
[73] J.F. Baugher, P.C. Taylor, T. Oja, P.J. Bray, Nuclear magnetic resonance powder patterns in the presence of completely asymmetric quadrupole and chemical shift effects: application to metavanadates, J. Chem. Phys. 50 (1969) 4914–4925, https://doi.org/10.1063/1.1670988.
[74] C.L. Turner, D. Koumoulis, G. Li, Z. Zujovic, R.E. Taylor, R.B. Kaner, Synthesis and characterization of aluminum diboride products using ^{27}Al, ^{11}B NMR and ab initio studies, J. Mater. Sci. 53 (2018) 3309.
[75] S. Strässle, J. Roos, M. Mali, H. Keller, J. Karpinski, ^{11}B NMR study of single-crystal MgB_2 in the normal conducting phase, Physica C 466 (2007) 168–173.
[76] N.N. Greenwood, A. Earnshaw, Chemistry of the Elements, Butterworth-Heinemann, 1997.
[77] B. Post, F.W. Glaser, D. Moskowitz, Transition metal diborides, Acta Metall. 2 (1) (1954) 20.
[78] G. Levchenko, A. Lyashchenko, V. Baumer, A. Evdokimova, V. Filippov, Yu Paderno, N. Shitsevalova, Preparation and some properties of ScB_2 single crystals, J. Solid State Chem. 179 (2006) 2949–2953.
[79] J.L. Hoard, R.E. Hughes, Elementary boron and compounds of higher boron content: structure, properties and polymorphism, in: E.L. Muetterties (Ed.), Ch 2 in the Chemistry of Boron and its Compounds, John Wiley and Sons Inc., New York, 1967.
[80] W. Martienssen, H. Warlimont, Springer Handbook of Condensed Matter and Materials Data, Springer-Verlag Berlin and Heidelberg, 2005, pp. 452–459, https://doi.org/10.1007/3-540-30437-1. Part 3.
[81] L.P. Cook, R. Klein, W. Wong-Ng, Q. Huang, R.A. Ribeiro, P.C. Canfield, Thermodynamics of MgB_2—by calorimetry and Knudsen thermogravimetry, IEEE Trans. Appl. Supercond. 15 (2) (2005) 3227.
[82] P. Villars, Pearson's Handbook: Crystallographic Data for Intermetallic Phases, ASM International, 1997.
[83] S.F. Matar, Electronic structure and chemical bonding within MgB_2 and related borides from first principles, Zeitschrift fur Naturforschung B 63 (6) (2008) 673–680, https://doi.org/10.1515/znb-2008-0613.
[84] S. Curtarolo, W. Setyawan, S. Wang, J. Xue, K. Yang, R.H. Taylor, L.J. Nelson, G.L. W. Hart, S. Sanvito, M. Buongiorno-Nardelli, N. Mingo, O. Levy, AFLOWLIB.ORG: a distributed materials properties repository from high-throughput ab initio calculations, Comput. Mater. Sci. 58 (2012) 227–235, https://doi.org/10.1016/j.commatsci.2012.02.002.
[85] T.Q. Wen, B. Ye, H. Liu, S. Ning, C.-Z. Wang, Y. Chu, Formation criterion for binary metal diboride solid solutions established through combinatorial methods, J. Am. Ceram. Soc. 103 (2020) 3338–3348, https://doi.org/10.1111/jace.16983.
[86] V.E. Zalizniak, O.A. Zolotov, K.A. Sidorov, Interatomic potential for metal diborides, Mol. Simul. 47 (12) (2021) 982–987, https://doi.org/10.1080/08927022.2021.1935925.
[87] G.E. Grechnev, A.S. Panfilov, A.V. Fedorchenko, V.B. Filippov, A.B. Lyashchenko, A.N. Vasiliev, Effect of pressure on the magnetic properties of CrB_2, Low Temp. Phys. 35 (2009) 531, https://doi.org/10.1063/1.3168639.
[88] Y. Wang, T. Plackowski, A. Junod, Specific heat in the superconducting and normal state (2-300K, 0-16 T), and magnetic susceptibility of the 38K superconductor MgB_2: evidence for a multicomponent gap, Physica C 355 (2001) 179.
[89] T.P. Onak, H. Landesman, R.E. Willams, The ^{11}B nuclear magnetic resonance chemical shifts and spin coupling values for various compounds, J. Phys. Chem. 63 (1959) 1533.
[90] J. Castaing, R. Caudron, G. Toupance, P. Costa, Electronic structure of transition metal diborides, Solid State Commun. 7 (1969) 1453.
[91] R.G. Barnes, R.B. Creel, D.R. Torgeson, Evidence for localized character of electronic structure in vanadium borides from ^{51}V nuclear magnetic resonance, Solid State Commun. 8 (1970) 1411.
[92] T.J. Bastow, Arsenic-75 NMR: knight shifts in arsenic metal, J. Phys. Condens. Matter 11 (1999) 569, https://doi.org/10.1088/0953-8984/11/2/019.
[93] M. Mali, J. Roos, A. Shengelaya, H. Keller, K. Conder, ^{25}Mg NMR study of the MgB_2 superconductor, Phys. Rev. B 65 (2002), 100518(R).
[94] A.R. Ferreira, DFT-GIPAW ^{27}Al NMR Simulations for intermetallics: accuracy issues and magnetic screening mechanisms, J. Phys. Chem. C 123 (2019) 9371–9381.
[95] R.J. Schoenberger, R.G. Barnes, NMR study of the antiferromagnetic transition in $V_xCr_{1-x}B_2$, AIP Conf. Proc. 5 (1972) 392–396, https://doi.org/10.1063/1.3699463.
[96] R.G. Barnes, T.P. Graham, Nuclear magnetic resonance in chromium metal, Phys. Rev. Letts. 8 (1962) 248.
[97] H. Kotegawa, K. Ishida, Y. Kitaoka, T. Muranaka, N. Nakagawa, H. Takagiwa, J. Akimitsu, Evidence for strong-coupling s-wave superconductivity in MgB_2: ^{11}B-NMR study of MgB_2 and the related materials, Physica C 378–381 (2002) 25–32.
[98] R.E. Snyder, J.W. Ross, D.P. Bunbury, Mossbauer effect measurements in ^{176,178,180}Hf, J. Phys. Part C: Solid State Phys. 1 (1968) 1662–1669 (b)10.
[99] E.N. Kaufmann, The electric field gradient at Ta in HfB_2, J. Phys. Chem. Solids. 34 (1973) 2025–2028.
[100] H. Haas, D.A. Shirley, Nuclear quadrupole interaction studies by perturbed angular correlations, J. Chem. Phys. 58 (1973) 3339–3355, https://doi.org/10.1063/1.1679661.
[101] R.B. Creel, S.L. Segel, R.J. Schoenberger, R.G. Barnes, D.R. Torgeson, Nuclear magnetic resonance study of the transition metal monoborides. II. Nuclear electric quadrupole and magnetic shift parameters of the metal nuclei in VB, CoB, and NbB, J. Chem. Phys. 60 (6) (1974) 2310–2322.

[102] S.J. Clark, M.D. Segall, C.J. Pickard, P.J. Hasnip, M.J. Probert, K. Refson, M. C. Payne, First principles methods using CASTEP, Zeitschrift fur Kristallographie 220 (5–6) (2005) 567–570.
[103] N.I. Medvedeva, A.L. Ivanovskii, J.E. Medvedeva, A.J. Freeman, D.L. Novikov, Electric field gradients in s-, p-, and d-metal diborides and the effect of pressure on the band structure and T_c in MgB_2, Phys. Rev. B 65 (2001) 052501.
[104] K. Choudhary, J.N. Ansari, I.I. Mazin, K.L. Sauer, Density functional theory-based electric field gradient database, Sci. Data 7 (2020) 362, https://doi.org/10.1038/s41597-020-00707-8.
[105] T.J. Bastow, M.I. Burgar, C. Maunders, Electric field gradients in metals: correlation of experimental results with ab initio calculation, Solid State Commun. 122 (11) (2002) 629.
[106] L.H. Bennett, R.E. Watson, G.C. Carter, Relevance of Knight shift measurements to the electronic density of states, Journal of Research of the National Bureau of Standards - A. Physics and Chemistry. 74A (4) (1970) 569–610.
[107] T. Lundström, B. Lönnberg, I. Westman, A study of the microhardness in the homogeneity ranges of NbB_2 and TaB_2, J. Less Common. Met. 96 (1984) 229–235.
[108] S. Indriss, P. Heitjans, J. Hattendorf, W.-D. Zeitz, T. Bredlow, Local electronic structure in MgB_2 from ^{12}B β-NMR, Phys. Rev. B 75 (2007) 024502.
[109] L.A. de Mello, H.M. Petrilli, S. Frota-Pessõa, The electric field gradient at the nucleus in HCP Zr and Hf, J. Phys. Condens. Matter 5 (1993) 8935.
[110] J. Castaing, P. Costa, Properties and uses of diborides. Chapter XI in Boron and Refractory Borides. Matkovich VI, Springer Verlag, New York, 1977, pp. 390–412.
[111] W.E. Blumberg, J. Eisinger, V. Jaccarino, B.T. Matthias, Nuclear magnetic resonance in scandium and lanthanum metal, Phys. Rev. Lett. 5 (2) (1960) 52.
[112] A. Bauer, A. Regnat, C.G.F. Blum, S. Gottlieb-Schönmeyer, B. Pedersen, M. Meven, S. Wurmehl, J. Kuneš, C. Pfleiderer, Low-temperature properties of single-crystal CrB_2, Phys. Rev. B 90 (2014) 064414.
[113] J.M. Ziman, Electrons and Phonons, Clarendon Press, Oxford, 1960.
[114] T. Leiner, N. Koutná, J. Janovec, M. Zelený, P.H. Mayrhofer, D. Holec, On energetics of allotrope transformations in transition-metal diborides via plane-by-plane shearing, Vacuum 215 (2023) 112329, https://doi.org/10.1016/j.vacuum.2023.112329.
[115] G. Bester, M. Fähnle, Interlayer contraction in MgB_2 upon replacement of Mg by Al: effect of the covalent bond energy, Phys. Rev. B 72 (2005) 094102, https://doi.org/10.1103/PhysRevB.72.094102.
[116] T. Morshedloo, M.R. Roknabadi, M. Behdani, First-principles study of the superconductivity in MgB_2 bulk and in its bilayer thin film based on electron–phonon coupling, Physica C 509 (2015) 1–4.
[117] R.G. Barnes, F. Borsa, S.L. Segel, D.R. Torgeson, Knight shift anisotropy in scandium and yttrium and nuclear quadrupole coupling in scandium, Phys. Rev. 137 (6A) (1965) A1828.
[118] C.H. Townes, B.P. Dailey, Determination of electronic structure of molecules from nuclear quadrupole effects, J. Chem. Phys. 17 (1949) 782–796.
[119] T.J. Bastow, A.J. Hill, A. Seeber, A. Trinchi, M.E. Smith, NMR determined interactions in CaB_6-structured metal hexaborides: correlation with structure and properties, Solid State Nucl. Magn. Reson. (2026) this issue.
[120] A.C. Gossard, V. Jaccarino, Boron nuclear magnetic resonance in rare earth intermetallic compounds, Proc Roy. Soc. 80 (1962) 877–881.
[121] W.A. Zdaniewski, N.L. Brungard, X-ray photoelectron spectroscopy of metallic diborides, Journal of the American Ceramics Society 75 (10) (1992) 2849.
[122] L. Brewer, The cohesive energies of the elements, LBL-3720 Rev. Preprint. US Energy Research and Development Administration under Contract W-7405-ENG-48 (1977) 1–18. https://escholarship.org/uc/item/08p2578m.
[123] G.V. Samsonov, Production and properties of scandium diboride, Dokl. Akad. Nauk SSSR 133 (6) (1960) 1344.
[124] K. Nakano, H. Matsubara, T. Imura, High temperature hardness of IVa diboride single crystals, J. Less Common. Met. 47 (1976) 259–264.
[125] S.N. Dub, S.M. Sichkar, V.A. Belous, G.N. Tolmacheva, P.I. Loboda, Y.I. Bogomol, G.P. Kysla, Mechanical properties of single crystals of transition metals diborides TMB_2 (TM = Sc, Hf, Zr, Ti). experiment and theory, J. Superhard Mater. 39 (5) (2017) 308.
[126] T. Prikhna, A. Lokatkina, V. Moshchil, P. Barvitskyi, O. Borimsky, S. Ponomaryov, R. Haber, T. Talako, Investigation of mechanical characteristics of materials based on refractory borides, Industrial and Technology Systems: Report on Research Projects 6/1 (56) (2020) 40–44. https://papers.ssrn.com/sol3/papers.cfm?abstract_id=3763009.
[127] S. Otani, M.M. Korsukova, T. Mitsuhashi, Floating zone growth and high-temperature hardness of NbB_2 and TaB_2 single crystals, J. Cryst. Growth 194 (1998) 430–433.
[128] L. Bzenko, T. Lundström, The high temperature hardness of ZrB_2 and HfB_2, J. Less Common. Met. 34 (1974) 273–278.
[129] Q.Liu H. Gan, S. Zhang, F. Wang, J. Cheng, X. Wang, S. Dong, Q. Tao, Y. Chen, P. Zhu, Robust hydrophobic materials by surface modification in transition-metal diborides, ACS Appl. Mater. Interfaces 13 (2021) 58162–58169.
[130] Y. Zhou, H. Xiang, Z. Feng, Z. Li, General trends in electronic structure, stability, chemical bonding and mechanical properties of ultrahigh temperature ceramics TMB_2 (TM = transition metal), J. Mater. Sci. Technol. 31 (2015) 285.
[131] D.M. Merriles, K.H. Tomchak, C. Nielson, M.D. Morse, Early transition metals strengthen the B_2 bond in MB_2 complexes, J. Am. Chem. Soc. 144 (17) (2022) 7557–7561, https://doi.org/10.1021/jacs.1c13709.
[132] B.C. Wyatt, S.K. Nemani, G.E. Hilmas, E.J. Opila, B. Anasori, Ultrahigh temperature ceramics for extreme environments, Nature Reviews 9 (11) (2024) 773–789, https://doi.org/10.1038/s41578-023-00619-0.
[133] Y. Pan, J. Zhu, Enhancing the Vickers hardness of yttrium borides through bond optimization, Mater. Today Commun. 38 (2024) 108428, https://doi.org/10.1016/j.mtcomm.2024.108428.
[134] Y. Chen, J. Rong, Z. Wang, Q. Tao, Q. Gan, F. Wang, Y. Ye, X. Liu, J. Cao, H. Fan, M. Wei, W. Zhang, P. Zhu, L. Yang, J. Yang, Tailoring the d-band center by borophene subunits in chromic diboride toward the hydrogen evolution reaction, Inorg. Chem. Front. 8 (2021) 5130–5138.
[135] P. Blaha, K. Schwarz, P.H. Dederichs, First-principles calculation of the electric-field gradient in hcp metals, Phys. Rev. B 37 (6) (1988) 2792.
[136] A.B. Peters, D. Zhang, S. Chen, C. Ott, C. Oses, S. Curtarolo, I. McCue, T. M. Pollock, S.E. Prameela, Materials design for hypersonics, Nat. Commun. 15 (2024) 3328.
[137] H. Eckert, Spying with spins on messy materials: 60 years of glass structure elucidation by NMR spectroscopy, Int. J. Appl. Glass Sci. 9 (2018) 167–187, https://doi.org/10.1111/ijag.12333.